Accepted: 22 October 2021

DOI: 10.1002/cpa.22113

RESEARCH ARTICLE

Generalization of waving-plate theory to multiple interacting swimmers

Peter J. Baddoo[1,†] | **Nicholas J. Moore**[2] | **Anand U. Oza**[3] | **Darren G. Crowdy**[4]

[1]Department of Mathematics, Massachusetts Institute of Technology, Cambridge, MA, United States

[2]Department of Mathematics, Colgate University, Hamilton, NY, United States

[3]Department of Mathematical Sciences, Center for Applied Mathematics and Statistics, New Jersey Institute of Technology, Newark, NJ, United States

[4]Department of Mathematics, Imperial College London, London, United Kingdom

Correspondence
Anand U. Oza, Department of Mathematical Sciences, Center for Applied Mathematics and Statistics, New Jersey Institute of Technology, Cullimore Hall, Newark, NJ 07102, United States.
Email: anand.u.oza@njit.edu

[†]This article is dedicated to the memory of the first author, Peter Baddoo, who sadly passed away while the article was in press.

Funding information
EPSRC, Grant/Award Number: EP/R014604/1; NSF, Grant/Award Numbers: DMS-2012560, DMS-2108839, DMS-1933403; Simons Foundation, Grant/Award Numbers: 524259, 587006

Abstract

Early research in aerodynamics and biological propulsion was dramatically advanced by the analytical solutions of Theodorsen, von Kármán, Wu and others. While these classical solutions apply only to isolated swimmers, the flow interactions between multiple swimmers are relevant to many practical applications, including the schooling and flocking of animal collectives. In this work, we derive a class of solutions that describe the hydrodynamic interactions between an arbitrary number of swimmers in a two-dimensional inviscid fluid. Our approach is rooted in multiply-connected complex analysis and exploits several recent results. Specifically, the transcendental (Schottky–Klein) prime function serves as the basic building block to construct the appropriate conformal maps and leading-edge-suction functions, which allows us to solve the modified Schwarz problem that arises. As such, our solutions generalize classical thin aerofoil theory, specifically Wu's waving-plate analysis, to the case of multiple swimmers. For the case of a pair of interacting swimmers, we develop an efficient numerical implementation that allows rapid computations of the forces on each swimmer. We investigate flow-mediated equilibria and find excellent agreement between our new solutions and previously reported experimental results. Our solutions recover and unify disparate results in the literature, thereby opening the door for future studies into the interactions between multiple swimmers.

CONTENTS

1. INTRODUCTION . . . 3812
2. MODELING . . . 3815
3. CONFORMAL MAPS AND THE PRIME FUNCTION . . . 3819
4. SOLUTION . . . 3825
5. RESULTS FOR PAIRS OF SWIMMERS . . . 3829
6. CONCLUSIONS . . . 3837
ACKNOWLEDGEMENTS . . . 3838
ORCID . . . 3839
REFERENCES . . . 3839
APPENDIX A: GENERAL HARMONIC MOTIONS . . . 3841
APPENDIX B: COMPARISON TO WU'S SOLUTION . . . 3842
APPENDIX C: DEGREES OF FREEDOM IN THE MAP . . . 3845
APPENDIX D: EXPLICIT EXPRESSIONS FOR THE REGULAR PART OF THE SOLUTION 3845
APPENDIX E: FAST COMPUTATION OF INTEGRALS COMPRISING THE SINGULAR PART OF THE SOLUTION . . . 3846
APPENDIX F: EXPRESSIONS FOR PHYSICAL QUANTITIES . . . 3848

1 | INTRODUCTION

The question of how animals propel themselves through a fluid, whether swimming or flying, is one that has captured the imagination of the scientific community and the public alike. This question becomes especially subtle when considering groups of self-propelled bodies, for example schools or flocks. Intriguingly, a number of observations [9, 32, 39, 43, 52] suggest that schooling fish could benefit from hydrodynamic interactions by realizing significant energy savings. Practitioners have already begun incorporating some of these principles into the design of next-generation technologies, such as underwater vehicles that emulate fish-like swimming by periodically actuating a set of propulsors attached to the sides of the main body [28, 58].

Experimental studies of interacting flapping foils in a water tank serve as valuable complements to observational studies of animal collectives, as the kinematics and flow conditions can be controlled. A natural starting point is the case of a pair of rigid foils that undergo two types of prescribed oscillatory motion at the same imposed frequency f_d with a possible phase offset ς (Figure 1): a linear motion perpendicular to the swimming direction (heaving) or a rotational motion about a fixed pivot point (pitching). The line connecting the two foils may be along the swimming direction (in-line), perpendicular to it (side-by-side) or at an angle (staggered). Studies on flapping foils in an imposed flow, held a fixed distance apart in an in-line configuration, have shown that the thrust on the downstream foil is sensitive to both the separation distance and phase offset [13, 30, 41, 61]. Meanwhile, studies on pitching foils in a side-by-side configuration [23, 29, 54] have suggested that the hydrodynamic thrust is maximized when the foils flap in antiphase, $\varsigma = \pi$.

Recent experiments [50, 53] have demonstrated that pairs of *freely-swimming foils* in an in-line configuration, initially at an arbitrary distance apart, spontaneously assume "schooling modes" in which the pair moves stably together at a fixed speed U_s while maintaining a constant separation distance ℓ. These studies have highlighted the importance of the "schooling number"

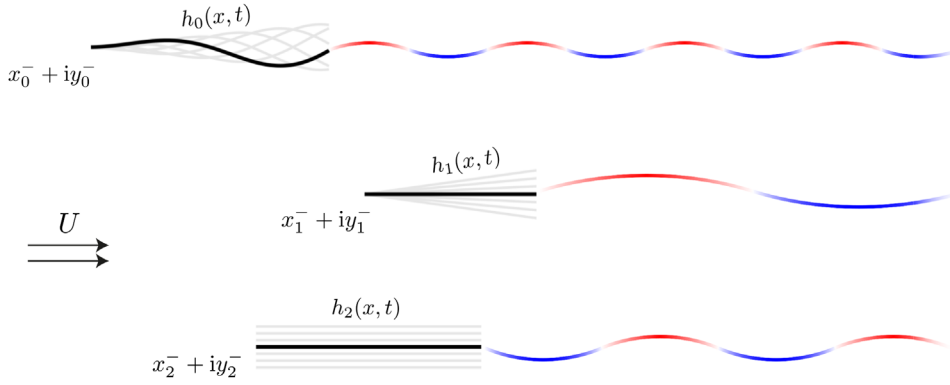

FIGURE 1 Schematic: a group of foils executing various flapping motions in a steady background flow of speed U. The foils have mean profile $h_m(x,t)$ and leading edges $x_m^- + \mathrm{i}y_m^-$. The motions depicted include undulation (h_0), pitching about the leading edge (h_1), and heaving (h_2). Each foil sheds a vortex sheet from its trailing edge, the strength of which is determined by the Kutta condition. This figure illustrates a staggered configuration, although any configuration is permitted.

$S = \ell f_d/U_s$, a dimensionless quantity that represents the number of flapping wavelengths separating the swimmers. Specifically, integer values of S correspond to spatially in-phase states in which the pair traces out the same path through space, while half-integer values indicate out-of-phase states. The experimental data across a range of flapping frequencies, amplitudes, and phase offsets may be approximated using the simple relation $S \approx n + \varsigma/(2\pi)$ where $n \in \mathbb{Z}$.

There are a number of numerical studies of pairs of flapping bodies in a viscous incompressible fluid, mostly in two dimensions (2D) and some in 3D. Studies on in-line flapping foils, held a fixed distance apart in an imposed flow, have shown that the thrust oscillates with both the distance between the foils ℓ and phase difference ς [3, 14, 22, 40, 48], in qualitative agreement with experiments. Studies on flapping foils in side-by-side arrangements have demonstrated that the hydrodynamic thrust is relatively large when the foils flap in antiphase [12, 24]. Methods that solve the Navier–Stokes equations directly, such as the immersed boundary method [22, 33, 40] or marker-and-cell scheme [7, 8], require a fine computational grid near the bodies in order to resolve thin boundary layers and are thus limited to moderate Reynolds numbers, $\mathrm{Re} = O(10^2) - O(10^3)$. Accurate and tractable simulations in regimes relevant to many swimming animals and biomimetic vehicles (e.g., $\mathrm{Re} = O(10^6) - O(10^7)$ for dolphins [58]) have thus remained elusive.

To overcome this limitation, some studies neglect the influence of viscosity and solve the Euler equations directly using vortex sheet methods [6, 25]: the bodies are represented using bound vortex sheets, and free vortex sheets are shed from the trailing edges. The limitation of such methods is that the length of a vortex wake grows with time, and the simulation quickly becomes intractable owing to the large number of vortices. The far-field wake is thus approximated by a small number of point vortices [6, 25], or contributions to the wake are removed after some prescribed timescale [34].

Generally, a detailed parametric study of the system is prohibitive, owing to the computational cost of simulations and the large number of control parameters involved. Even for the relatively simple situation of a pair of rigid foils heaving in a viscous fluid, control parameters include the dimensionless amplitudes (Strouhal numbers), the reduced flapping frequencies, the streamwise

and lateral distances between foils, the phase offset, and the Reynolds number. If different foil motions are permitted (e.g., pitching), or if the foil surfaces can deform due to elasticity [45, 46], the parameter space becomes even larger. Clearly, analytical solutions, if feasible, would help conquer this vast parameter space.

Analytical progress is possible in the case of 2D flow over an infinitesimally-thin foil (flat plate) undergoing small-amplitude motions and shedding a non-deforming planar wake from its trailing edge, a setting in which the Euler equations may be linearized. This so-called "thin-airfoil theory" was pioneered in the early twentieth century by Theodorsen [56] and von Kármán and Sears [60], who obtained closed-form expressions for the lift and moment of pitching and heaving plates in a uniform background flow. Garrick [27] extended the method outlined by von Kármán and Burgers [59] to derive expressions for the propulsive thrust on such plates. These results were recently extended by Fernandez-Feria [26], who considered the influence of the wake vorticity on the entire plate as opposed to the leading edge alone.

Wu [62] proposed an alternative approach to explicitly calculate the hydrodynamic forces on a deformable plate undergoing time-harmonic undulations. Crucially, Wu worked directly with the pressure field rather than the velocity field, which considerably simplifies the analysis: the pressure is continuous everywhere in the domain except across the plate, while the tangential component of the velocity is discontinuous across the vortex wake. The small-amplitude theories of Theodorsen [56], von Kármán and Sears [60], Garrick [27], and Wu have advanced our understanding of swimming animals [55] and biomimetic vehicles [47], whose propulsors often execute flapping motions with amplitude small relative to their body length.

While Wu's framework has been profitably extended to account for unsteady forward motion [63] and foil flexibility [44–46], it has not yet been extended to account for multiple flapping bodies. The problem of a pair of rigid foils heaving in an in-line configuration was treated in an approximate fashion by Ramananarivo et al. [53] (Supplemental Material), who, following the approach of Wu and Chwang [64], first calculated the wavy flow generated by the leading foil, and then calculated the hydrodynamic thrust on the follower immersed in that background flow. Similarly, recent work has furnished approximate formulas for the forces and moments on a pair of rigid [4] and deformable [5] foils. These works neglect the contribution of the follower's vortex wake on the leader's wake for the sake of simplicity, an approximation expected to be valid only when the streamwise separation between the foils is large. In particular, such an approximation cannot be applied to the side-by-side configuration.

Here, we present a natural extension of Wu's theory to account for multiple swimming bodies, with no such approximations made regarding the streamwise spacing between them. The newly developed theory leverages recent advances on conformal mappings of multiply-connected domains using the so-called Schottky-Klein prime function. An outline of the paper is as follows. In Section 2, we present the governing equations for a collection of plates undergoing oscillatory kinematics in a uniform background flow, following Wu's original framework [62]. In Section 3, we introduce the prime function and its relevant properties. In Section 4, we demonstrate how this function can be used to solve the governing equations for an arbitrary number of plates, and explicate solutions for the special case of two plates. In Section 5, we explore the physical consequences of our solutions for pairs of heaving, pitching and waving plates, plotting the pressure fields and deducing the dependence of the time-averaged thrust on both the distance between the plates and the flapping phase difference. The results are compared to existing experimental and numerical results in the literature. Conclusions and future directions are discussed in Section 6.

2 | MODELING

The basic hydrodynamic model employed here follows closely that of Wu [62] and Moore [44, 46], with the appropriate modifications needed to model multiple swimmers. Consider a group of $M+1$ foils swimming together at speed U_s through an otherwise quiescent fluid of density ρ. The foils may have different chord lengths, with c chosen as a characteristic value (e.g., the mean). In the present paper, the foils all swim in the same direction and at the same speed. The general framework, however, permits small deviations in swimming speed and direction, an extension that will be explored in future work. The swimmers' propulsion arises from a flapping motion driven at a characteristic frequency f_d. We employ the same non-dimensionalization as in earlier work [44, 46], with distance scaled on $c/2$, time on $1/f_d$, velocity on $cf_d/2$, and pressure on $\rho c^2 f_d^2/4$. With the appropriate Gallilean transformation, the swimmers can be considered stationary and embedded in a flow of dimensionless free-stream value $U = 2U_s/(cf_d)$, as illustrated in Figure 1.

Each plate executes transverse motions with its mean surface expressed as $h_m(x,t)$, where the subscript denotes the m-th plate for $m = 0, \dots, M$. The key assumption underlying this theory is that the characteristic amplitude of the transverse motion, A_s, is small compared to the body lengthscale c. In the dimensionless variables, both h_m and $\partial_x h_m$ are $\mathcal{O}(\epsilon)$, where $\epsilon = A_s/c \ll 1$. We associate the physical domain with a complex variable $z = x + \mathrm{i}y$. The edges of the swimmers are located at $z_m^{\pm} = x_m^{\pm} + \mathrm{i}y_m^{\pm}$ where $\pm$ corresponds to the trailing and leading edge, respectively. While the fluid velocity is permitted to have an integrable singularity at each leading edge, the Kutta condition requires that the velocity remain finite at each trailing edge. Each plate sheds a vortex sheet that extends from its trailing edge indefinitely, $z \to +\infty$, the strength of which is prescribed by the Kutta condition. These sheets represent the vorticity that is accumulated and eventually shed from the viscous boundary layer surrounding each foil. Apart from this vortex-shedding effect, the fluid is assumed to be inviscid.

Upon linearizing the Euler equation in small-amplitude motion, the incompressible (divergence-free) velocity field $\boldsymbol{u} = (U+u, v)$ satisfies

$$(\partial_t + U\partial_x)\boldsymbol{u} = \nabla\phi \tag{2.1}$$

where $\phi(z,t) = p_\infty - p$ and p is the (non-dimensional) pressure with far-field value p_∞. Taking the divergence of (2.1) and enforcing incompressibility of $\boldsymbol{u}$ implies that ϕ is a harmonic function throughout the domain,

$$\nabla^2\phi = 0. \tag{2.2}$$

Thus, ϕ admits a harmonic conjugate which gives rise to an analytic function

$$f(z,t) = \phi(z,t) + \mathrm{i}\psi(z,t). \tag{2.3}$$

In the literature, f is known as the complex acceleration potential, due to the fact that $\nabla\phi$ yields the fluid acceleration as expressed in (2.1). Alternatively, ϕ can be regarded simply as a negative, normalized pressure field. In terms of the complex velocity field $w(z,t) = u(z,t) - \mathrm{i}v(z,t)$, (2.1) implies the relationship

$$\partial_z f = (\partial_t + U\partial_z)w. \tag{2.4}$$

An important distinction exists regarding the domains over which f and w enjoy analyticity. The acceleration potential, f, is analytic everywhere except on the plates themselves. In particular, f is analytic across each of the semi-infinite vortex sheets, whereas w possesses branch cuts along these sheets. Thus, working with f as the primary state variable considerably simplifies the analysis as the vortex sheets do not require special attention. These vortex sheets are certainly present in the model (indeed, without them, there would be no thrust), but they need not be computed explicitly. If desired, they can be computed as a post-processing step.

On each plate, the fluid velocity must satisfy a no-flux condition, which, upon linearization, reads

$$v_m(x,t) = (\partial_t + U\partial_x)h_m(x,t) \qquad \text{for } x_m^- < x < x_m^+, \tag{2.5}$$

where v_m is the vertical velocity on the m-th plate. Combining (2.4) and (2.5) furnishes the condition

$$\partial_x \psi(x + \mathrm{i}y_m, t) = -(\partial_t + U\partial_x)^2 h_m(x,t) \qquad \text{for } x_m^- < x < x_m^+. \tag{2.6}$$

We antidifferentiate the boundary data (2.6) to obtain the functions

$$\Psi_m(x,t) = -\int_{x_m^-}^{x} (\partial_t + U\partial_x)^2 h_m(x',t)\mathrm{d}x' \qquad \text{for } x_m^- < x < x_m^+. \tag{2.7}$$

Thus, on each boundary component, ψ matches Ψ_m up to an integration constant. These constants, which may be different on each boundary component, will later be determined by a compatibility condition.

In addition, the velocity must vanish far upstream and the pressure must tend to the reference value in the far-field, giving conditions:

$$|w(z,t)| \to 0 \qquad \text{as} \quad x \to -\infty, \tag{2.8}$$

$$\phi(z,t) \to 0 \qquad \text{as} \quad |z| \to \infty. \tag{2.9}$$

Due to geometric considerations, the tangential fluid velocity possesses a square-root singularity at the leading edge z_m^- of each plate [35, 62]. Moreover, the velocity at the trailing-edge z_m^+ must remain finite due to the Kutta condition. We thus obtain two endpoint conditions on each plate:

$$w(z,t) = O\left(\frac{1}{\sqrt{z - z_m^-}}\right) \qquad \text{as} \quad z \to z_m^-, \tag{2.10}$$

$$|w(z_m^+,t)| < \infty. \tag{2.11}$$

In summary, we seek a complex acceleration potential $f(z,t)$, analytic in the domain D_z exterior to the $M+1$ plates, whose imaginary part matches (2.7) up to a constant of integration on each plate and whose real part satisfies the far-field condition (2.9). Furthermore, the complex velocity $w(z,t)$, related to $f(z,t)$ through (2.4), must satisfy boundary condition (2.5), far-field condition (2.8), and endpoint conditions (2.10)–(2.11).

2.1 | Harmonic motions

With the model established for general motions, we now consider the special case of harmonic motions. That is, each plate oscillates harmonically in time, with its own amplitude and phase. Owing to linearity, it suffices to consider the case of a single oscillation frequency f_d; the case of multiple oscillation frequencies can be obtained by Fourier superposition, as shown in Appendix A. Scaling time on $1/f_d$, the motion of the m-th foil is expressed as

$$h_m(x,t) = h_m^c(x)\cos(2\pi t) + h_m^s(x)\sin(2\pi t) \tag{2.12}$$

where t is the dimensionless time.

We similarly decompose $f(z,t)$ and $w(z,t)$ and introduce the vector quantities

$$\boldsymbol{f} = \begin{bmatrix} f^c(z) \\ f^s(z) \end{bmatrix}, \qquad \boldsymbol{w} = \begin{bmatrix} w^c(z) \\ w^s(z) \end{bmatrix}. \tag{2.13}$$

In this notation, (2.4) becomes

$$\partial_z \boldsymbol{f}(z) = 2\pi \boldsymbol{J}\boldsymbol{w}(z) + U\partial_z \boldsymbol{w}(z) \tag{2.14}$$

where

$$\boldsymbol{J} = \begin{bmatrix} 0 & 1 \\ -1 & 0 \end{bmatrix}. \tag{2.15}$$

We remark that $\boldsymbol{J}$ can be viewed as a matrix representation of the imaginary unit since $\boldsymbol{J}^2 = -\boldsymbol{I}$, where $\boldsymbol{I}$ is the identity matrix. The eigendecomposition of $\boldsymbol{J}$ gives the convenient formula

$$\mathrm{e}^{\sigma \boldsymbol{J} z} = \begin{bmatrix} \cos(\sigma z) & \sin(\sigma z) \\ -\sin(\sigma z) & \cos(\sigma z) \end{bmatrix} \tag{2.16}$$

which is directly analogous to Euler's formula for $e^{\sigma j z}$. Some previous studies [44, 46, 62] used an imaginary unit $j = \sqrt{-1}$, distinct from the unit i so that $\mathrm{i} \times j \neq -1$. We instead use the above matrix representation to avoid the (potentially significant) confusion of having two distinct imaginary units, which would be compounded by the task of working in multiply-connected domains in the complex plane.

Momentarily treating $\boldsymbol{f}(z)$ as given, (2.14) can be viewed as a first-order ODE system for $\boldsymbol{w}(z)$, whose solution is given by

$$\boldsymbol{w}(z) = \frac{1}{U}\mathrm{e}^{-\sigma \boldsymbol{J} z} \int_{-\infty}^{z} \mathrm{e}^{\sigma \boldsymbol{J} z'} \partial_z \boldsymbol{f}(z')\mathrm{d}z' \tag{2.17}$$

where $\sigma = 2\pi/U$ is called the reduced frequency. In terms of physical parameters, $\sigma = \pi f_d c/U_s$, so the reduced frequency measures the ratio of the flapping period to the time required for the free-stream flow to travel across a typical plate.

The boundary data (2.7) can be written as

$$\boldsymbol{\Psi}_m = \begin{bmatrix} \Psi_m^c \\ \Psi_m^s \end{bmatrix} = -U^2 \int_{x_m^-}^{x} \left(\sigma \boldsymbol{J} + \boldsymbol{I}\frac{\mathrm{d}}{\mathrm{d}x'}\right)^2 \boldsymbol{h}_m(x')\mathrm{d}x' \qquad \text{for } x_m^- < x < x_m^+, \tag{2.18}$$

where $\boldsymbol{h}_m = [h_m^c \quad h_m^s]^T$.

2.2 | The solution for a single plate

Here, we briefly rederive Wu's single-plate result [62] in a way that will naturally generalize to multiple plates. After non-dimensionalizing, the single plate occupies the slit $z \in [-1, 1]$. Following Wu, we associate the physical z-plane with a parametric ζ-plane via the Joukowski map

$$\mathcal{Z}(\zeta) = \frac{1}{2}\left(\frac{1}{\zeta} + \zeta\right). \tag{2.19}$$

This function conformally maps the unit disk in the ζ-plane to the exterior of the plate in the z-plane. The unit circle C_0 maps to the plate, with the trailing and leading edges corresponding to $\zeta_0^{\pm} = \pm 1$. We let $F(\zeta, t) \equiv f(z, t)$ represent the complex acceleration potential in the ζ-plane. The behavior of the map (2.19) near $\zeta = \zeta_0^- = -1$, combined with (2.4) and (2.10), implies a simple pole in the complex potential $F(\zeta, t)$:

$$F(\zeta, t) \sim \frac{\mathrm{i}a_0(t)}{\zeta + 1} \qquad \text{as } \zeta \to -1. \tag{2.20}$$

Since the velocity of the plate is finite, so too is $\mathrm{Im}[F(\zeta, t)]$ on C_0 by the boundary condition (2.6), which implies that a_0 is real. Note that $F(\zeta, t)$ must be finite as $\zeta \to \zeta_0^+ = +1$ by the Kutta condition (2.11).

At this point, we depart from Wu's derivation and introduce notation that may seem extraneous for the single-plate problem, but that will generalize nicely to the multiply-connected setting. In particular, the function

$$\hat{\mathcal{K}}(\zeta, \alpha) = -\frac{\mathrm{i}\alpha}{\zeta - \alpha} \tag{2.21}$$

with $\alpha = \zeta_0^- = -1$, has the form required to capture the singularity in (2.20). We therefore resolve $F(\zeta, t)$ into singular and regular components:

$$F(\zeta, t) = a_0(t)\hat{\mathcal{K}}(\zeta, -1) + L(\zeta, t), \qquad a_0 \in \mathbb{R}, \tag{2.22}$$

where $L(\zeta, t)$, the regular part, is analytic inside the unit disc and *finite* on the boundary C_0. Importantly, the function $\hat{\mathcal{K}}(\zeta, -1)$ takes constant imaginary part on the boundary: $\mathrm{Im}[\hat{\mathcal{K}}(\zeta, -1)] = 1/2$ for $\zeta \in C_0$. Therefore, taking the imaginary part of (2.22), evaluating on the boundary and applying (2.6)–(2.7) gives

$$\mathrm{Im}[L(\zeta, t)] = \Psi_0(\zeta, t) \qquad \text{for } \zeta \in C_0, \tag{2.23}$$

where we have fixed a constant of integration without losing generality.

Thus, $L(\zeta, t)$ is a (single-valued) analytic function that is finite on the boundary and whose imaginary part takes prescribed values on C_0. Mathematically, this is known as a (modified) *Schwarz problem* [16]. In the simply-connected case, the solution is given by the Poisson formula [2, 18]:

$$L(\zeta, t) = \frac{1}{2\pi}\oint_{C_0} \Psi_0(\zeta', t)\left[\frac{\zeta' + \zeta}{\zeta' - \zeta}\right]\frac{\mathrm{d}\zeta'}{\zeta'} + D(t), \qquad D(t) \in \mathbb{R}. \tag{2.24}$$

The (time-dependent) constant $D(t)$ is chosen to satisfy the far-field condition (2.9). Equation (2.24) can be discretized by a quadrature method of the reader's choice, and we therefore consider the regular part of the solution to be completely determined.

All that remains is to determine the coefficient $a_0(t)$ of the singular part in (2.22). It suffices to evaluate the no-flux condition at a single point on the plate. For example, if the plate executes harmonic motions, we may take the imaginary part of the contour integral (2.17) and apply the no-flux condition (2.5) to yield an expression for a_0 in terms of Bessel functions. The details of how to derive these Bessel functions, and further connections to Wu's solution are explicated in Appendix B.

In summary, we deployed four steps in the solution of Wu's problem:

(1) Conformally map the circular domain to the physical domain;
(2) Construct a function, $\hat{\mathcal{K}}(\zeta, \alpha)$, that has the appropriate leading-edge singularity and, simultaneously, assumes constant imaginary part on the boundary;
(3) Solve the Schwarz problem to determine the regular part of the solution;
(4) Calculate the coefficient $a_0(t)$ by evaluating the no-flux condition at a single point on the boundary.

In Section 3 and Section 4, we will explain how to generalize each of these steps to multiple plates.

We remark that Wu did not explicitly use the Poisson formula (2.24) to solve for the acceleration potential, but instead matched coefficients in a series expansion [62]. The advantage of the Poisson-formula representation, however, is that, once the requisite mathematical objects are introduced, it easily generalizes to any connectivity (Section 3.4). Furthermore, Wu's series expansion can be recovered directly from the Poisson formula above; indeed, a series expansion could be viewed as a convenient quadrature method for (2.24). We provide some relevant details in Appendix B.

3 | CONFORMAL MAPS AND THE PRIME FUNCTION

We now introduce the main mathematical machinery that will be used to generalize Wu's solution to multiple swimmers. For a single swimmer, the familiar Joukowski map (2.19) associates the physical domain with the unit disc in the ζ-plane. For multiple swimmers, the unit disc is no longer appropriate, but an extension of the Riemann mapping theorem guarantees the existence of a conformal mapping from a multiply connected circular domain D_ζ of the kind shown in Figure 2 to the unbounded fluid region exterior to $M + 1$ swimming plates. The domain D_ζ is the unit ζ disc with M smaller circular discs excised, the smaller discs having centers $\{\delta_m | m = 1, \dots, M\}$ and radii $\{q_m | m = 1, \dots, M\}$. The outer boundary of D_ζ, the unit circle, will be denoted by C_0, its interior circular boundaries by $\{C_m | m = 1, \dots, M\}$. Here we exploit this generalized mapping theorem and carry out an analysis that is a direct theoretical extension of Wu's single plate analysis to multiple swimming plates.

The appropriate mathematical machinery exists: a general framework for solving problems in multiply connected planar domains has been described in a recent monograph [18] and is based on consideration of a so-called *prime function* (also known as the "Schottky–Klein prime function" [11]), denoted here by

$$\omega(\zeta, \alpha), \tag{3.1}$$

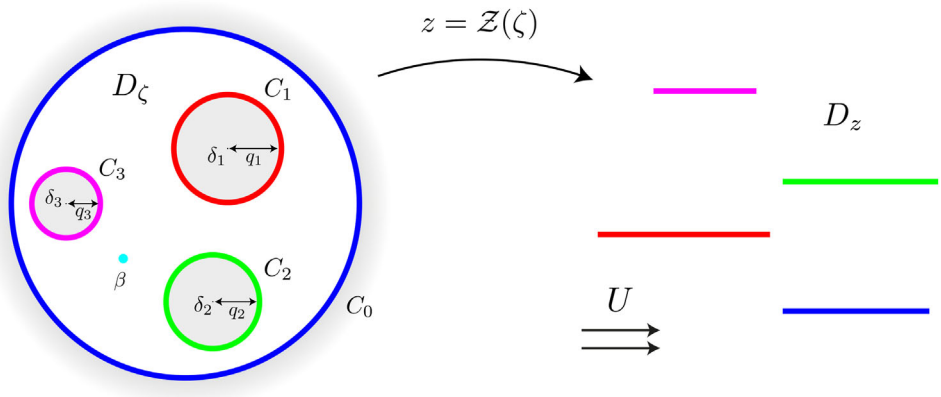

FIGURE 2 The conformal map. We map a canonical circular domain D_ζ of connectivity $M + 1$ to the unbounded fluid region D_z exterior to $M + 1$ swimming plates. The circular domain D_ζ is characterized by the centers $\{\delta_m | m = 1, \dots, M\}$ and radii $\{q_m | m = 1, \dots, M\}$ of M discs with boundaries C_m excised from a unit disc with boundary C_0.

that can naturally be associated with any given domain D_ζ. The notation (3.1) is convenient, but note that it hides the dependence of the prime function on the parameters $\{\delta_m, q_m\}$ characterizing the domain D_ζ. The prime function is a classical special function, but its significance for solving problems in multiply connected domains – such as the swimming plate problem of interest here – had been missed until recently. The prime function for a disc with no holes is the simple function

$$\omega(\zeta, \alpha) = \zeta - \alpha. \tag{3.2}$$

Invoking this important fact in the general formulation to follow will retrieve Wu's results for a single swimming plate.

The treatment in [18] demonstrates that the theory of the prime function associated with D_ζ is connected to potential theory in that domain; indeed, the prime function can be defined as a double limit of a so-called third kind differential built from a suitable potential theoretic Green's function defined in D_ζ. While the Green's function is the more familiar object to applied scientists, it turns out that the lesser-known prime function is the more versatile object for representing the solution of many different applied problems involving multiply connected domains (see [18] Part 2). Numerical codes are now available [1] for efficient and accurate calculation of the prime function associated with a given circular domain D_ζ [20].

One of the main arguments [18] for the importance, and theoretical significance, of the prime function is that many results familiar in a simply connected setting – here, Wu's single-plate analysis – can be generalized in a natural way to the multiply connected setting. Presenting the specific details of this generalization for Wu's swimming plate problem is the aim of this paper.

3.1 | Modified Green's functions and the prime function

With the prime function $\omega(.,.)$ associated with a multiply connected circular domain D_ζ understood to be a well-defined and computable function, we now record all the requisite results needed

to generalize Wu's single-plate analysis to multiple swimming plates. These results are reported here without proof; full details can be found in [18].

An important observation for present purposes concerns the *modified Green's function* $G_0(\zeta,\alpha)$ in D_ζ that satisfies

$$\nabla^2 G_0(\zeta,\alpha) = -\delta(\zeta-\alpha), \qquad \zeta,\alpha \in D_\zeta \tag{3.3}$$

and assumes constant values on each boundary component of D_ζ. It can be expressed in terms of the prime function associated with D_ζ as

$$G_0(\zeta,\alpha) = \mathrm{Im}[\mathcal{G}_0(\zeta,\alpha)], \qquad \mathcal{G}_0(\zeta,\alpha) = \frac{1}{2\pi \mathrm{i}} \log\left(\frac{\omega(\zeta,\alpha)}{|\alpha|\omega(\zeta,1/\overline{\alpha})}\right). \tag{3.4}$$

Since D_ζ is $(M+1)$-connected, there are M additional modified Green's functions conveniently expressed as

$$G_m(\zeta,\alpha) = \mathrm{Im}[\mathcal{G}_m(\zeta,\alpha)], \qquad \mathcal{G}_m(\zeta,\alpha) = \frac{1}{2\pi \mathrm{i}} \log\left(\frac{\omega(\zeta,\alpha)}{|\alpha|\omega(\zeta,\theta_m(1/\overline{\alpha}))}\right), \tag{3.5}$$

where

$$\theta_m(\zeta) = \delta_m + \frac{q_m^2 \zeta}{1-\overline{\delta_m}\zeta}, \qquad m = 1,\dots,M \tag{3.6}$$

are Möbius mappings associated with each boundary circle. The modified Green's functions satisfy

$$\nabla^2 G_m(\zeta,\alpha) = -\delta(\zeta-\alpha), \qquad \zeta,\alpha \in D_\zeta, \qquad m = 1,\dots,M \tag{3.7}$$

and all assume constant values on the boundary components of D_ζ. The difference between the various modified Green's functions lies in whether their analytic extensions $\{\mathcal{G}_m(\zeta,\alpha)\}$ are single-valued around the boundary circles: the function $\mathcal{G}_m(\zeta,\alpha)$ is single-valued around all boundaries of D_ζ except for C_m [18]. Crowdy [15] first introduced the functions (3.5) in the context of calculating the lift forces on a set of aerofoils in a steady uniform flow (see also Section 4.10 of [18]).

These modified Green's functions enable us to solve the swimming plate problem for multiple interacting plates. In particular, we use the modified Green's functions to generalize the first three steps outlined at the end of Section 2.2: constructing the conformal map, constructing the leading-edge singularity functions, and solving the modified Schwarz problem.

Before proceeding it is useful to introduce the function

$$\mathcal{K}(\zeta,\alpha) \equiv \alpha \frac{\partial}{\partial \alpha} \log \omega(\zeta,\alpha), \tag{3.8}$$

which has a singularity at α of the form

$$\mathcal{K}(\zeta,\alpha) \sim -\frac{\alpha}{\zeta-\alpha}. \tag{3.9}$$

This function is important in the general framework [18] and also plays a prominent role in our analysis. Indeed, the complete solution to our problem can be phrased exclusively in terms of the function $\mathcal{K}$.

3.2 | Parallel slit maps

First, it can be shown [18, 21] that within a class of so-called *parallel slit maps* is the function given by

$$-2\pi \mathrm{i}\left[\frac{\partial}{\partial \alpha}-\frac{\partial}{\partial \overline{\alpha}}\right]\mathcal{G}_m(\zeta,\alpha), \qquad m=0,1,\ldots,M. \tag{3.10}$$

The point α, assumed to be strictly inside D_ζ, is mapped to infinity in an image plane. Moreover, all circles $\{C_m | m=0,1,\ldots,M\}$ are transplanted to slits of finite length all parallel to the real axis – hence the designation "parallel slit maps". These properties follow directly from those of the modified Green's functions and the observation that

$$\frac{\partial}{\partial \alpha}-\frac{\partial}{\partial \overline{\alpha}}=\frac{\partial}{\partial(\mathrm{i}\alpha_y)}, \tag{3.11}$$

where $\alpha=\alpha_x+\mathrm{i}\alpha_y$. Since $\mathcal{G}_m$ has constant imaginary part when $\zeta\in\partial D_\zeta$, so too does (3.10), as it is the parametric derivative of $-2\pi\mathrm{i}\mathcal{G}_m$ with respect to the purely imaginary parameter $\mathrm{i}\alpha_y$. It is also easily verified that the map (3.10) has a simple pole with unit residue at $\zeta=\alpha$. Consequently, the map transplants D_ζ to the unbounded region exterior to $M+1$ slits all parallel to the real axis in the image plane; see [18] for more details.

For $m=0$, for example, (3.8) can be used to write (3.10) as

$$\varphi_0(\zeta,\alpha)=-\frac{1}{\alpha}\mathcal{K}(\zeta,\alpha)+\frac{1}{\overline{\alpha}}\mathcal{K}(\zeta,1/\overline{\alpha}), \tag{3.12}$$

up to terms independent of ζ. The mapping $\varphi_0(\zeta,\alpha)$ has a constant imaginary part when ζ lies on any boundary circle of D_ζ. Thus, any function

$$\mathcal{Z}(\zeta)=A\varphi_0(\zeta,\beta)+B, \qquad A\in\mathbb{R}^+, B\in\mathbb{C}, \tag{3.13}$$

serves as a mapping from D_ζ to $M+1$ swimming plates parallel to the real axis with β now used to denote the preimage of the point at infinity for consistency (see Figure 2). Given the locations of the end points of $M+1$ swimming plates, namely,

$$[z_m^-, z_m^+], \qquad m=0,1,\ldots,M, \tag{3.14}$$

the parameters $A, B, \{\delta_m, q_m | m=1,\ldots,M\}$ can be determined by solving a parameter problem. Specifically, we denote the preimages of $z_m^\pm$ as $\zeta_m^\pm$, each pair being on one of the boundary circles. Then, in order that the images are the end points of a slit, necessary conditions are

$$\mathcal{Z}(\zeta_m^\pm)=z_m^\pm, \qquad \left.\frac{\mathrm{d}\mathcal{Z}}{\mathrm{d}\zeta}\right|_{\zeta_m^\pm}=0, \qquad m=0,1,\ldots,M. \tag{3.15}$$

Since the functional form of $\mathcal{Z}(\zeta)$ is known from (3.13) up to a finite set of parameters, the set (3.15) is a finite system of nonlinear equations for those parameters. In the problem considered here, where the arrangement of swimming plates is fixed at the outset, these parameters can be solved for as a set-up step in the calculation. The number of parameters matches the number of constraints, as shown in Appendix C.

Once the parameters are found, the mapping (3.13) is precisely the function we need to generalize the classical Joukowski map (2.19) used by Wu. To see this explicitly, note that, for a single

plate ($M = 0$),

$$\omega(\zeta, \alpha) = \zeta - \alpha, \qquad \mathcal{K}(\zeta, \alpha) = -\frac{\alpha}{\zeta - \alpha} \tag{3.16}$$

and (3.13) becomes

$$\mathcal{Z}(\zeta) = A\left[\frac{1}{\zeta - \beta} - \frac{1}{\zeta - 1/\overline{\beta}}\right] + B = A\left[\frac{1}{\zeta - \beta} + \frac{1}{\overline{\beta}}\frac{1}{(1 - \overline{\beta}\zeta)}\right] + B. \tag{3.17}$$

Setting $A = 1/2$ and $B = -A/\overline{\beta}$, and then letting $\beta \to 0$ retrieves the Joukowski map (2.19).

3.3 | Leading-edge singularity functions

Geometrically, as α tends to a boundary point of D_ζ, the functions (3.10) give a class of so-called parallel slit mappings that transplant the boundary circle on which α sits to an infinite line parallel to the finite-length slit images of all other circles. Such functions are not of interest to us as conformal mappings, but they are useful for describing the pressure singularities present at the leading edge of each wing.

Suppose, for example, that α tends to C_0, i.e., $\alpha \to e^{\mathrm{i}\vartheta}$ for some $0 \le \vartheta < 2\pi$. Then $\alpha \to 1/\overline{\alpha}$ and

$$\varphi_0(\zeta, \alpha) \to -\mathrm{e}^{-\mathrm{i}\vartheta}\mathcal{K}(\zeta, \alpha) + \mathrm{e}^{\mathrm{i}\vartheta}\mathcal{K}(\zeta, \alpha) = 2\mathrm{i}\mathcal{K}(\zeta, \alpha)\sin\vartheta. \tag{3.18}$$

Recall that, for $\zeta \neq \alpha$, $\varphi_0(\zeta, \alpha)$ has constant imaginary part on all boundary circles of D_ζ. Therefore, (3.18) shows that $\mathrm{i}\mathcal{K}(\zeta, \alpha)$ has constant imaginary part on the M boundary circles $\{C_m | m = 1, \dots, M\}$ and, away from the singularity at α, also on C_0.

If, on the other hand, $\alpha \to \delta_m + q_m\mathrm{e}^{\mathrm{i}\vartheta}$ for some $m = 1, \dots, M$, an analogous analysis of the limit of (3.10) allows us to deduce that the function

$$\varphi_m(\zeta, \alpha) = -\frac{1}{\alpha}\mathcal{K}(\zeta, \alpha)\left[1 + \frac{\partial}{\partial\overline{\alpha}}\theta_m(1/\overline{\alpha})\right] \tag{3.19}$$

has constant imaginary part on each boundary circle; here we have used the fact that if α lies on C_m then $\theta_m(1/\overline{\alpha}) = \alpha$. But, from (3.6),

$$\frac{\partial}{\partial\overline{\alpha}}\theta_m(1/\overline{\alpha}) = -\mathrm{e}^{2\mathrm{i}\vartheta} \tag{3.20}$$

which implies that

$$\varphi_m(\zeta, \alpha) = \frac{2\sin\vartheta}{q_m}\left[\mathrm{i}\left(\frac{\alpha - \delta_m}{\alpha}\right)\mathcal{K}(\zeta, \alpha)\right], \tag{3.21}$$

which shows that, for $\zeta \neq \alpha$, the function in square brackets has constant imaginary part on each boundary circle (different constant values on different circles). Formula (3.21) reduces to (3.18) when $q_m = 1, \delta_m = 0$.

In summary, if we define $\delta_0 = 0$, we can say that when α tends to *any* boundary circle C_m, the function

$$\hat{\mathcal{K}}(\zeta, \alpha) \equiv \mathrm{i}\left(\frac{\alpha - \delta_m}{\alpha}\right)\mathcal{K}(\zeta, \alpha), \qquad m = 0, 1, \dots, M \tag{3.22}$$

has a singular real part with a simple pole at $\zeta = \alpha$ and (finite) constant imaginary part when $\zeta \in \partial D_\zeta$ (different constant values on different boundary circles). This fact will be useful in resolving the leading-edge pressure singularities.

For the case of a single plate, $M = 0$, using (3.16) with $\delta_0 = 0$ and $\alpha = -1$, the function (3.22) becomes

$$\hat{\mathcal{K}}(\zeta, -1) = \frac{\mathrm{i}}{\zeta + 1} \tag{3.23}$$

which is precisely the function used by Wu [62] to account for a pressure singularity on the swimming plate, as described in Section 2.2.

3.4 | Solution of the modified Schwarz problem in D_ζ

Determining the complex acceleration potential can be viewed as a *modified Schwarz problem* [16, 18], that is, the problem of finding a single-valued analytic function with prescribed real (or imaginary) part on the boundary. In multiply connected domains, the solution to such a problem can be written explicitly in terms of the prime function [16, 18]. In the present context, we seek an analytic function $F(\zeta) = \phi + \mathrm{i}\psi$ whose imaginary part is known up to a constant on all boundary components. Eventually, F will represent the regular part of the complex acceleration potential (specifically, $L(\zeta, t)$ in (4.3)), but for the purposes of this section we use F simply to refer to an analytic function. Multiplication by $-\mathrm{i}$ allows us to map to the standard modified Schwarz problem:

$$\mathrm{Re}[-\mathrm{i}F(\zeta)] = \mathrm{Im}[F(\zeta)] = \psi = \begin{cases} \Psi_0, & \text{on} \quad C_0, \\ \Psi_m + d_m, & \text{on} \quad C_m, \ m = 1, \dots, M, \end{cases} \tag{3.24}$$

where $\{\Psi_m | m = 0, 1, \dots, M\}$ are considered known (via (2.7) in the present context), and the M constants $\{d_m | m = 1, \dots, M\}$ must satisfy a set of M *compatibility conditions* for a single-valued solution to exist [16, 18]. Given that these conditions are met, the solution is

$$\begin{aligned} F(\zeta) &= \frac{1}{2\pi}\int_{\partial D_\zeta} \psi(\zeta')\left[\mathrm{d}\log\omega(\zeta', \zeta) + \mathrm{d}\log\overline{\omega}(\overline{\zeta'}, 1/\zeta)\right] + D \\ &= \frac{1}{2\pi}\int_{\partial D_\zeta} \psi(\zeta')\left[\mathcal{K}(\zeta, \zeta')\frac{\mathrm{d}\zeta'}{\zeta'} + \overline{\mathcal{K}}(1/\zeta, \overline{\zeta}')\frac{\mathrm{d}\overline{\zeta'}}{\overline{\zeta'}}\right] + D, \qquad D \in \mathbb{R}, \end{aligned} \tag{3.25}$$

where $\overline{g}(\zeta, \alpha) \equiv \overline{g(\overline{\zeta}, \overline{\alpha})}$ denotes the Schwarz conjugate of g. Here, integration over the multi-component boundary ∂D_ζ is defined as

$$\int_{\partial D_\zeta} = \oint_{C_0} - \sum_{m=1}^{M} \oint_{C_m} \tag{3.26}$$

where $\oint$ denotes integration over a closed contour in the counter-clockwise direction. The integral formula (3.25) in terms of the prime function was first written down in [16]; see also Chapter 13 of [18]. In the single-plate case $M = 0$ and on use of (3.16), Equation (3.25) reduces to the Poisson formula (2.24) and thus recovers Wu's single-plate solution.

4 | SOLUTION

Having introduced the necessary mathematical objects, we now solve the multiple-swimmer problem introduced in Section 2. Specifically, we seek an analytic function $F(\zeta, t)$ (the complex acceleration potential) whose imaginary part matches (2.7) up to a constant of integration on each boundary component of ∂D_ζ and whose real part satisfies the far-field condition (2.9). Furthermore, the complex velocity, related to the acceleration potential through (2.4), must satisfy the boundary condition (2.5), far-field condition (2.8), and edge conditions (2.10)–(2.11). We present the solution decomposition (Section 4.1) and the regular part of the solution (Section 4.2) for general motions. We then present the singular part of the solution (Section 4.3) for time-harmonic motions (Section 2.1), for which (2.18) sets the boundary conditions on the acceleration potential and (2.17) relates it to the velocity field.

4.1 | Solution decomposition

As seen in (3.15), the multi-connected conformal map (3.13) has the same quadratic structure near the endpoints of each plate $[z_m^-, z_m^+]$ as does the Joukowski map (2.19). Thus, due to (2.4) and the square-root singularity in the velocity field (2.10), the complex acceleration potential $F(\zeta, t)$ must possess a simple pole at the pre-image of each leading edge $\zeta = \zeta_m^-$ for $m = 0, \dots, M$, just as it does in the simply-connected case. The function $\hat{\mathcal{K}}(\zeta, \zeta_m^-)$ defined in (3.22) also has a simple pole at $\zeta = \zeta_m^-$, allowing us to extract the singularities from F as follows:

$$F(\zeta, t) = \sum_{m=0}^{M} a_m(t)\hat{\mathcal{K}}(\zeta, \zeta_m^-) + L(\zeta, t) + D(t). \tag{4.1}$$

What remains, $L(\zeta, t)$, is an analytic function that is *finite* on all boundary components. We thus refer to $L(\zeta, t)$ as the regular part of the solution, and $D = D(t)$ is an overall constant that enforces the far-field condition (2.9). The coefficients $a_m(t)$ physically represent the strength of the leading-edge suction forces on each plate. Importantly, since both F and $\hat{\mathcal{K}}$ have finite imaginary part but singular real part on the boundary circles, the coefficients a_m must be real.

4.2 | Regular part of the solution

We showed in Section 3.3 that each function $\hat{\mathcal{K}}(\zeta, \zeta_m^-)$ assumes a constant imaginary part on each boundary component of D_ζ. Therefore, evaluating the imaginary part of (4.1) on the boundary gives

$$\mathrm{Im}[L(\zeta, t)] = \Psi_m(\zeta, t) + d_m(t), \qquad \zeta \in C_m,\ m = 0, \dots, M \tag{4.2}$$

where Ψ_m is boundary data that is known through (2.7), and the (time-dependent) constants d_m arise from two sources: first, from anti-differentiating (2.6) to obtain Ψ_m, and second from the evaluation of $\hat{\mathcal{K}}(\zeta, \zeta_m^-)$ on each boundary. In our formulation, it is unnecessary to distinguish between these two contributions, so we combine them into a single term d_m. One of these can be absorbed into the overall constant D, and so, without loss of generality, we take $d_0 = 0$.

Now, (4.2) takes the form of a modified Schwarz problem as discussed in Section 3.4. An integral formula for the solution therefore follows from (3.25):

$$L(\zeta, t) = \frac{1}{2\pi} \int_{\partial D_\zeta} \left(\Psi_m(\zeta', t) + d_m(t)\right) \left[\mathcal{K}(\zeta, \zeta') \frac{\mathrm{d}\zeta'}{\zeta'} + \overline{\mathcal{K}}(1/\zeta, \overline{\zeta'}) \frac{\mathrm{d}\overline{\zeta'}}{\overline{\zeta'}}\right], \tag{4.3}$$

where the (time-dependent) constants $d_m(t)$ can be determined by enforcing compatibility conditions. The coefficients $a_m(t)$ of the singular terms are not determined by this formula and must be treated separately.

We note that an analogous procedure applies in the case of harmonic motions (Section 2.1), with Ψ_m replaced by its vectorized equivalent (2.18). We then express the solution (4.3) as $\boldsymbol{L} = [L^c(\zeta) \quad L^s(\zeta)]^T$. Closed-form expressions for $\boldsymbol{L}$ – that is, without integrals – are available for the simple case of in-phase heaving motions, as shown in Appendix D.

4.3 | Singular part of the solution

With the regular part of the solution given by (4.3), all that remains is to determine the singular part. For simplicity, we consider the case of harmonic motions. By decomposition (4.1), the singular part is fully specified by the $2(M+1)$ real constants $\boldsymbol{a}_m = [a_m^c \quad a_m^s]^T$ for $m = 0, \dots, M$.

To determine these constants, we will construct a linear system of $2(M+1)$ equations. To this end, we sample the plate boundaries at $M+1$ points labeled $z_m = x_m + \mathrm{i}y_m$, with one point on each plate. Substituting (4.1) into (2.17) and enforcing the no-flux boundary condition (2.5) at $z = z_m$ yields the equation

$$\mathrm{Im}\left[-\sum_{n=0}^{M} \frac{1}{U} \int_{-\infty}^{z_m} \mathrm{e}^{\sigma \boldsymbol{J}(z - z_m)} \boldsymbol{a}_n \frac{\mathrm{d}\hat{\mathcal{K}}}{\mathrm{d}z}(\zeta(z), \zeta_n^-)\, \mathrm{d}z\right] = \boldsymbol{v}(z_m) + \boldsymbol{q}(z_m) \tag{4.4}$$

for $m = 0, \dots, M$, where

$$\boldsymbol{v}(z_m) = U\left(\sigma \boldsymbol{J} + \boldsymbol{I}\frac{\mathrm{d}}{\mathrm{d}x}\right)\boldsymbol{h}_m(x_m) \tag{4.5}$$

and

$$\boldsymbol{q}(z_m) = \mathrm{Im}\left[\frac{1}{U} \int_{-\infty}^{z_m} \mathrm{e}^{\sigma \boldsymbol{J}(z - z_m)} \frac{\mathrm{d}\boldsymbol{L}}{\mathrm{d}z}(\zeta(z))\, \mathrm{d}z\right]. \tag{4.6}$$

Note that $\boldsymbol{v}(z_m)$ is known because the plates' kinematics are prescribed, and $\boldsymbol{q}(z_m)$ is already known since it depends only on the regular part $\boldsymbol{L}$ of the solution. Therefore, the right side of (4.4) is known.

As established in Section 4.1, the coefficients $\boldsymbol{a}_n$ are real and can thus be moved outside the brackets in (4.4). Therefore, we obtain the linear system

$$\boldsymbol{D}\boldsymbol{a} = \boldsymbol{b}, \tag{4.7}$$

where

$$\boldsymbol{a} = \begin{bmatrix} \boldsymbol{a}_0 \\ \vdots \\ \boldsymbol{a}_M \end{bmatrix}, \qquad \boldsymbol{b} = \begin{bmatrix} \boldsymbol{v}(z_0) + \boldsymbol{q}(z_0) \\ \vdots \\ \boldsymbol{v}(z_M) + \boldsymbol{q}(z_M) \end{bmatrix}, \tag{4.8}$$

and

$$\boldsymbol{D}_{m,n} = -\frac{1}{U}\mathrm{Im}\left[\mathrm{e}^{-\sigma \boldsymbol{J} z_m}\int_{-\infty}^{z_m}\mathrm{e}^{\sigma \boldsymbol{J} z}\frac{\mathrm{d}\hat{\mathcal{K}}}{\mathrm{d}z}(\zeta, \zeta_n^-)\mathrm{d}z\right] \tag{4.9}$$

is the 2×2 block of $\boldsymbol{D}$ in position (m, n). Solving the linear system (4.7) yields the values of the $2(M+1)$ constants $\boldsymbol{a}$.

In the simply-connected case, the integrals in (4.4) and (4.6) can be expressed in terms of Bessel functions, but analytical expressions are unavailable in the general multiply-connected case. We therefore evaluate these integrals numerically using a rapidly-converging quadrature scheme detailed in Appendix E. Taken together, Equations (4.1), (4.3), and (4.7) comprise the solution for the acceleration potential $F(\zeta, t)$.

4.4 | Two swimming plates

The case of two swimming plates, corresponding to $M = 1$, is of special interest for two reasons. First, the interesting physics of interaction is likely to be well captured by just two interacting plates. The second reason is that the general formulation presented thus far affords significant mathematical simplifications in the case $M = 1$ because the preimage domain D_ζ can be taken to be the concentric annulus $\rho < |\zeta| < 1$, for which

$$\delta_1 = 0, \qquad q_1 = \rho < 1. \tag{4.10}$$

On a practical level this means that use of numerical codes to compute the prime function can be avoided, and the following (suitably truncated) infinite product and sum representations of the requisite functions can be used directly. We emphasize that our general formulation, and the formulas derived in Sections 4.1–4.3, pertain to *any number* of swimming plates. We plan to use our general formulation to investigate the case of three or more swimming plates in future work.

It can be shown – see Chapters 5 and 14 of [18] – that for the concentric annulus $\rho < |\zeta| < 1$,

$$\omega(\zeta, \alpha) = -\frac{\alpha}{C^2}P(\zeta/\alpha), \qquad C = \prod_{n=1}^{\infty}(1-\rho^{2n}), \tag{4.11}$$

where

$$P(\zeta) = (1-\zeta)\prod_{n=1}^{\infty}(1-\rho^{2n}\zeta)(1-\rho^{2n}/\zeta) \tag{4.12}$$

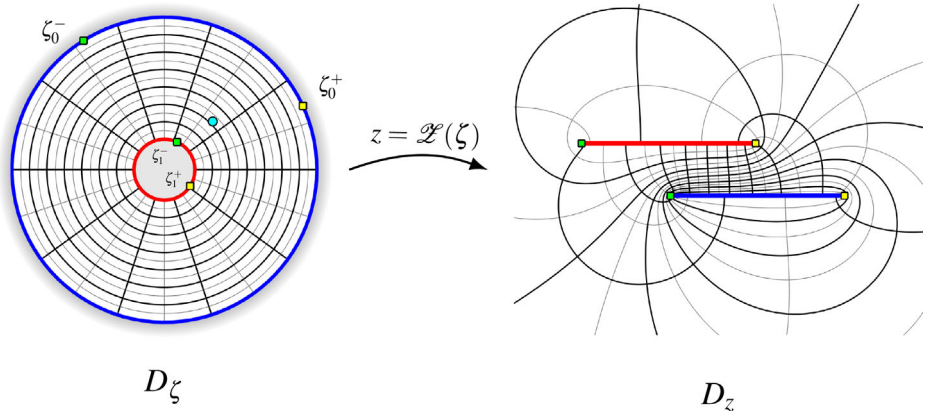

FIGURE 3 An example of a parallel slit map $\mathcal{Z}(\zeta)$ between doubly connected domains. The annulus is mapped to the exterior of two finite, parallel slits. The blue (red) circle is mapped to the blue (red) slit. The cyan dot in the D_ζ plane represents the preimage of infinity, β. The preimages of the edges of the slits are denoted by the green (ζ_i^-) and yellow (ζ_i^+) circles for the leading and trailing edges, respectively. In this plot, the conformal modulus is taken to be $\rho = 0.05$ and $\beta = \sqrt{\rho}e^{i\pi/4}$.

is a (uniformly) convergent product for $0 \leq \rho < |\zeta| < 1$. This function satisfies the functional relations [18]:

$$P(\rho^2\zeta) = -\zeta^{-1}P(\zeta) = P(1/\zeta). \tag{4.13}$$

Substituting (4.11) and (4.12) into the definition of $\mathcal{K}$ given in (3.8), we obtain

$$\mathcal{K}(\zeta,\alpha) = \frac{1}{1-\zeta/\alpha} + \sum_{n=1}^{\infty}\left\{\frac{\rho^{2n}\zeta/\alpha}{1-\rho^{2n}\zeta/\alpha} - \frac{\rho^{2n}\alpha/\zeta}{1-\rho^{2n}\alpha/\zeta}\right\}. \tag{4.14}$$

Figure 3 shows the corresponding conformal map $\mathcal{Z}(\zeta)$, as given by (3.13), for a typical set of parameters. We note that choosing $|\beta| = \sqrt{\rho}$ leads to a pair of plates of equal length. For a given configuration of plates, it is necessary to determine ρ and $\arg(\beta)$ by solving the parameter problem described in Section 3.2. Alternatively, a range of configurations may be produced by sweeping across values of these parameters, as we do in Section 5.3. We note that the special case of real (imaginary) β produces the in-line (stacked) configuration considered in Section 5.

Equation (4.13) can be used to write (4.3) as

$$\begin{aligned} L(\zeta,t) = &\frac{1}{2\pi}\oint_{C_0}\Psi_0(\zeta',t)\left[2\mathcal{K}(\zeta,\zeta')-1\right]\frac{\mathrm{d}\zeta'}{\zeta'} \\ &-\frac{1}{2\pi}\oint_{C_1}(\Psi_1(\zeta',t)+d_1(t))[2\mathcal{K}(\zeta,\zeta')]\frac{\mathrm{d}\zeta'}{\zeta'} + D(t), \end{aligned} \tag{4.15}$$

where $D(t) \in \mathbb{R}$. This is an integral formula for the solution of the modified Schwarz problem in the concentric annulus [18]. The single compatibility condition which ensures that the acceleration potential is single-valued (as discussed in [16]) is

$$\oint_{C_0}\Psi_0(\zeta,t)\frac{\mathrm{d}\zeta}{\zeta} = \oint_{C_1}[\Psi_1(\zeta,t)+d_1(t)]\frac{\mathrm{d}\zeta}{\zeta}, \tag{4.16}$$

which affords an explicit expression for $d_1(t)$ in terms of Ψ_0 and Ψ_1. For the two-plate case it turns out that use of the integral formula (4.15) can be circumvented, since a computationally efficient method based on Laurent series can be used instead. That method, which we use here, is described in appendix D of [19].

The results in this section may readily be connected to Wu's single-plate theory [62] by taking the limit $\rho \to 0$. Specifically, this limit reduces the annulus to the unit disc, and formula (4.15) reduces to the Poisson integral formula (2.24). A further simplification of the general theory is that, since $\delta_0 = \delta_1 = 0$, (4.14) may be used to show that (3.22) reduces to the singularity function (3.23) used by Wu.

5 | RESULTS FOR PAIRS OF SWIMMERS

Using the solution derived in Section 4.4, we now present the pressure fields (Section 5.1) and hydrodynamic thrust (Section 5.2 and Section 5.3) associated with pairs of swimmers, and give physical interpretations of our results.

5.1 | Pressure fields

Our formulation casts the entire hydrodynamic problem in terms of the complex acceleration potential, $f(z,t) = \phi(z,t) + \mathrm{i}\psi(z,t)$, whose real part $\phi(z,t)$ is simply the (negative and normalized) pressure field. Other quantities, such as velocity and vorticity, can be extracted from $f(z,t)$ if desired, but they are not needed to determine the hydrodynamic forces on swimmers. Hence, in this section, we focus on the pressure field as the main physical diagnostic for gaining insights into fluid-mediated interactions between two swimmers.

Figures 4a–4c show instantaneous pressure fields surrounding two foils that heave in phase. The figures show a few different configurations: (A) inline, (B) side-by-side, and (C) a diagonal configuration. Figures 5a–5c show similar plots but for foils that heave in anti-phase. Distinct features in the surrounding pressure fields are apparent.

First consider the inline and in-phase case shown in Figure 4a. As indicated in the figure, the free-stream flow is left to right, so we refer to the foil on the left as the leader and the right as

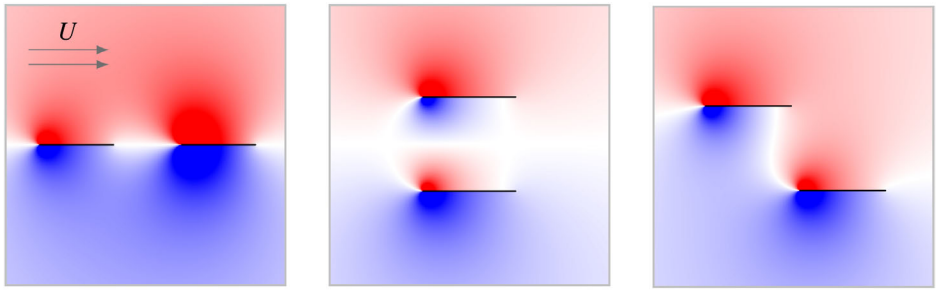

FIGURE 4 Instantaneous pressure fields for three different foil configurations. The foils are heaving in phase at a reduced frequency of $\sigma = 1$. At the instant shown, both foils are in the upward phase of their motion, experiencing high pressure (red) along the top surface and low pressure (blue) along the bottom.

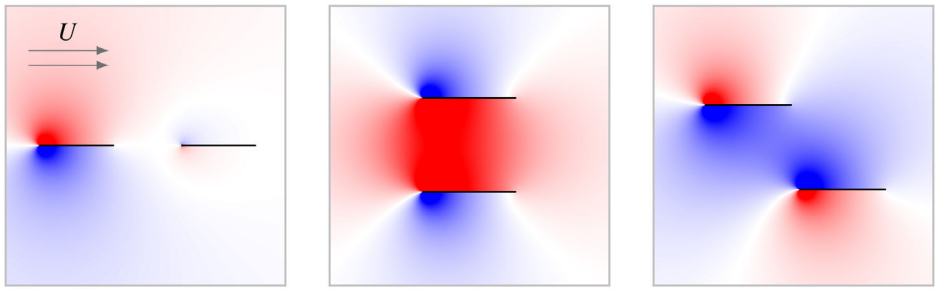

FIGURE 5 Instantaneous pressure fields for three different foil configurations. The foils are heaving in anti-phase at a reduced frequency of $\sigma = 1$.

the follower. At the instant shown, both foils are in the upward phase of their motion and thus experience high pressure (red) along the top surface and low pressure (blue) along the bottom. The interaction with the leader's wake evidently increases the pressure differential across the follower, thereby enhancing its own lift and thrust forces. Whether the follower's hydrodynamic forces are strengthened or weakened by the leader's wake depends on many details, such as the separation distance and relative flapping phase, as will be explored more thoroughly in what follows.

Figures 4b and 4c reveal features of the surrounding pressure fields for the side-by-side and diagonal arrangements. We note that in-phase heaving foils in the side-by-side arrangement (Figure 4b) effectively move the fluid in between them as a cohesive unit. This coherent motion reduces the pressure differential due to less relative motion between foil and fluid which, as will be shown in Section 5.3, ultimately reduces the thrust that is generated.

The case of anti-phase heaving, shown in Figure 5a–5c, is perhaps more subtle. For the inline configuration (Figure 5a), the leader is heaving upwards and the follower downwards at the instant shown. Hence, the leader (follower) experiences high pressure along its top (bottom) surface, with the pressure differential across the follower being significantly weakened by the interaction. The side-by-side case (Figure 5b) is of particular interest as it is connected to the ground-effect problem of a plate swimming above an impenetrable wall [10]: by symmetry, there is no vertical flux through the horizontal axis lying midway between the two plates so the bottom plate acts as the image of the top one. At the instant shown, both foils are heaving towards the center, thus squeezing the fluid in between and creating a region of high pressure. As we will see in Section 5.3, this squeezing action significantly enhances the thrust that is generated. The staggered case (Figure 5c) shows a combination of the features from the inline and side-by-side arrangements. At the instant shown, the staggered foils are heaving away from one another.

We remark that the singular term in (4.1) can produce large pressure values in the vicinity of each foil's leading edge, as are visible in a few of these figures. How visible the effect is depends on details like which phase is shown. These singularities also contribute to the net thrust through the so-called leading-edge suction, as detailed in Appendix F.

5.2 | Hydrodynamic thrust for the inline configuration

We now further quantify the inline, in-phase configuration by showing in Figure 6 the thrust produced by the foils, time-averaged over the flapping period. The thrust is calculated using the

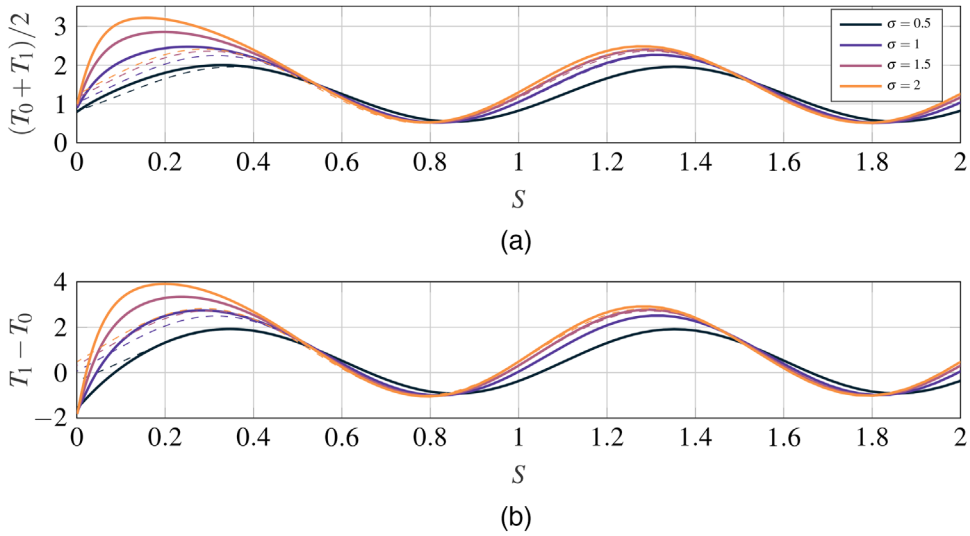

FIGURE 6 The normalized average (a) and difference (b) of thrusts for a pair of inline foils that are heaving in-phase. The full solutions are plotted in thick lines whereas the asymptotic solution of [53] is plotted in dashed lines.

formulas derived in Appendix F. In this section and the sequel, we only consider time-averaged quantities and thus drop the angle brackets notation of Appendix F (e.g., $\langle T_0 \rangle$). We introduce the so-called schooling number to quantify the horizontal spacing ℓ between the foils [51, 53]: $S = \ell f_d / U_\infty = \ell \sigma / \pi c$, where ℓ is the (dimensional) distance between the trailing edge of the leader and the leading edge of the follower. Thus, the schooling number represents the spacing between the foils normalized by the wake wavelength.

Figure 6a shows the average thrust $(T_1 + T_0)/2$ produced by the leader (T_0) and follower (T_1) as a function of the schooling number S. Here, $(T_1 + T_0)/2$ is normalized by the thrust produced by an isolated foil. The figure reveals that $(T_1 + T_0)/2 > 1$ for most schooling numbers, meaning that the two foils generate greater thrust when flapping together than they would in isolation. There is also a smaller range (roughly $0.65 < S < 1.0$, the precise values depending on σ) for which the interaction leads to reduced thrust. For S outside of that range, the thrust enhancement can be substantial. In the most extreme case, $S = 0.15$ and $\sigma = 2$, the interacting foils generate more than triple the thrust they would if they were performing the same motions in isolation. The greatest thrust enhancement occurs for closely-spaced foils, roughly $S = 0.1 - 0.3$, and for relatively large σ. The peak in thrust enhancement is seen to reoccur periodically, roughly $S = 1.3, 2.3, 3.3, \ldots$, due to the periodicity of the wake.

Figure 6(b) shows the thrust difference, $T_1 - T_0$, normalized by the thrust produced by a single foil performing the same motions. For most schooling numbers, $T_1 - T_0 > 0$, indicating that the follower produces greater thrust than the leader. In these cases, the follower reaps a net benefit from interacting with the leader's wake. There is also a small range (roughly $S = 0.65 - 1.0$) for which $T_1 - T_0 < 0$, and the leader's wake effectively exerts a drag on the follower. In both Figures 6a and 6b, we also plot the asymptotic solution of [53], which is valid for large S. It is evident that, for all values of σ considered, the asymptotic solution agrees well with our computation for large S, thus validating our results.

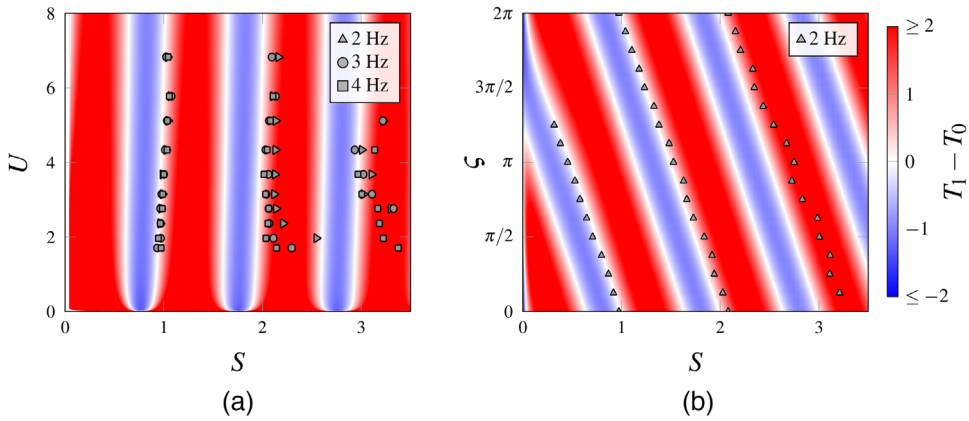

FIGURE 7 (a) The thrust difference $T_1 - T_0$ for a pair of inline foils that are heaving in-phase. Horizontal cuts of the plot (fixed $U = 2\pi/\sigma$) correspond to the curves shown in Figure 6b. The points indicate experimental data on pairs of freely swimming flapping foils in a water tank [53]. Different symbols correspond to the flapping frequencies indicated in the legend, and the flapping amplitude ranges from $0.05c$ to $0.4c$. (b) The thrust difference $T_1 - T_0$ for a pair of inline foils heaving with the indicated phase difference ς. The points indicate experimental data [50] for foils flapping with frequency 2 Hz and amplitude $0.4c$. The value of σ corresponds to the midpoint of the range of horizontal velocities $U_\infty = 18 - 28$ cm/s reported in experiments.

Importantly, Figure 6b offers some insight into the dynamics of self-propelled swimmers. For example, if the follower were to begin at a spacing of $S = 1.5$ behind the leader, it would generate greater thrust and thus begin to catch up. The follower would continue to close the distance until the two thrusts become equal, $T_1 = T_0$, which is seen to occur at approximately $S = 0.95 - 1.05$ with only weak dependence on σ. Hence, our computation predicts an equilibrium spacing of $S \approx 1$ between the free swimmers.

The results in Figure 6b are extended in Figure 7a to a larger range of schooling numbers S and velocities $U = 2\pi/\sigma$. The white regions of the plots indicate parameters for which the leader and follower produce equal thrust, $T_1 = T_0$, while blue (red) indicates the leader (follower) producing greater thrust. By the foregoing arguments, our theory predicts stable equilibrium spacings to occur at $S \approx n$ for $n \in \mathbb{N}$. This prediction exhibits excellent agreement with experimental data (points in Figure 7a) on the equilibrium configurations adopted by freely swimming heaving foils in an in-line configuration [53]. Specifically, the data points for a range of flapping frequencies and amplitudes lie near the stable zero-contours of the thrust difference, $T_1 - T_0$, that were calculated by the theory. The same is true for Figure 7b, wherein we explore the influence of the flapping phase difference ς and compare with experimental data [50]. Note that values of S corresponding to unstable zero-contours, with $T_1 > T_0$ (red) to the left and $T_1 < T_0$ (blue) to the right, were not realized in experiments. The theory and experiments agree well throughout the parameter space, especially for smaller schooling numbers $S < 2.5$ where the agreement is quantitative. For larger S, the theory still predicts the qualitative trend of the data, but the agreement is less accurate, likely due to the increased importance of viscous effects far downstream of the leader's wake. Indeed, experimental measurements [50, 53] have shown the strength of the wake to decay exponentially over a timescale of a few seconds in water, and these effects are not accounted for in the present inviscid theory.

5.3 | Thrust on staggered configurations

Unlike previous investigations, the present theory does not constrain the swimmers to the inline configuration. Thus, Figures 8–10 expand the discussion of the preceding section to interacting swimmers having arbitrary lateral positions. In these figures, the position of one foil is fixed at the origin, and points in the plane correspond to the leading edge of the second foil. The average thrust (top row), difference in thrusts (middle row), and average efficiency (bottom row) are shown in color for three different phase differences, $\varsigma = 0, \pi/2, \pi$ (moving left to right). Each point in the plane corresponds to the computation of a different swimmer-pair interaction, with different points representing different configurations. Altogether, roughly 21,000 swimmer-pair interactions are represented in each of these figures. The narrow gray region surrounding the origin is excluded from consideration, since, here, the close proximity of the foils degrades the numerical accuracy of the solutions.

The top row of Figure 8 shows the average thrust, $(T_1 + T_0)/2$, generated by the pair of *heaving* foils for the three phase differences ($\varsigma = 0, \pi/2$, and π). The kinematics are given by $h_m(x,t) = \cos(2\pi t + m\varsigma)$. Viewing the case $\varsigma = 0$ along the positive x-axis recovers the inline

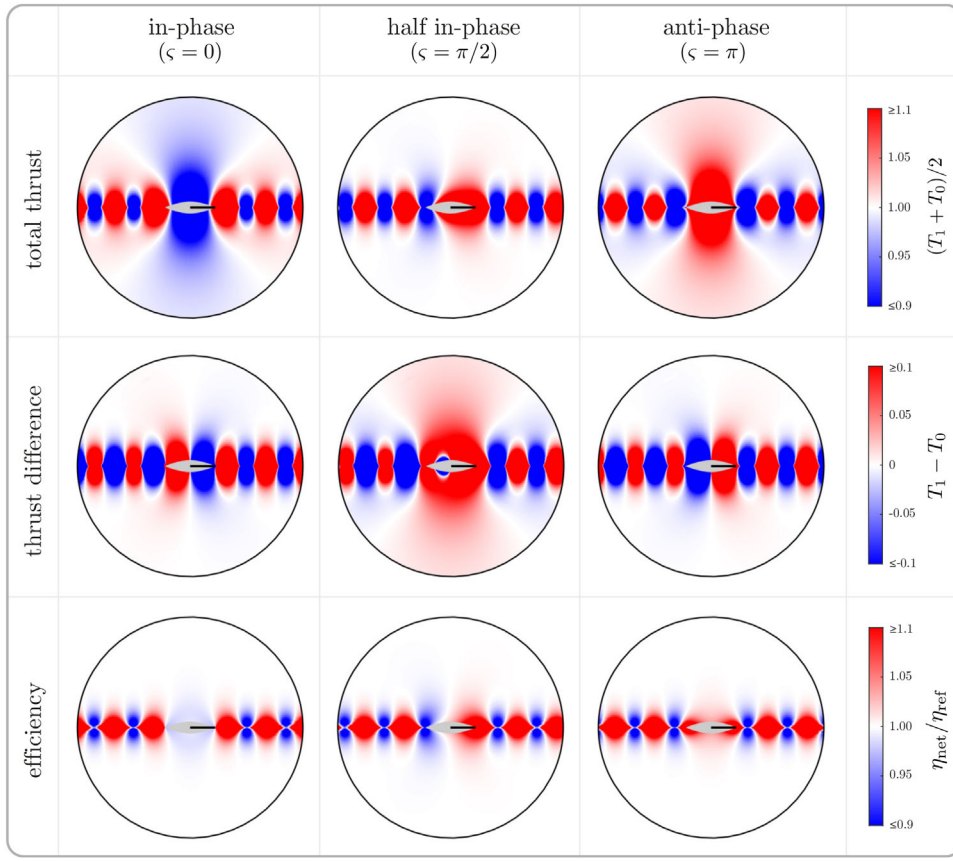

FIGURE 8 The dependence of dynamic quantities on the relative positions of a pair of heaving foils. We plot the total thrust, thrust difference, and efficiency for foils at the indicated phase differences and $\sigma = 2$. One plate ("0") is indicated by the black line, and colored points in the plane correspond to the leading edge of the other plate ("1").

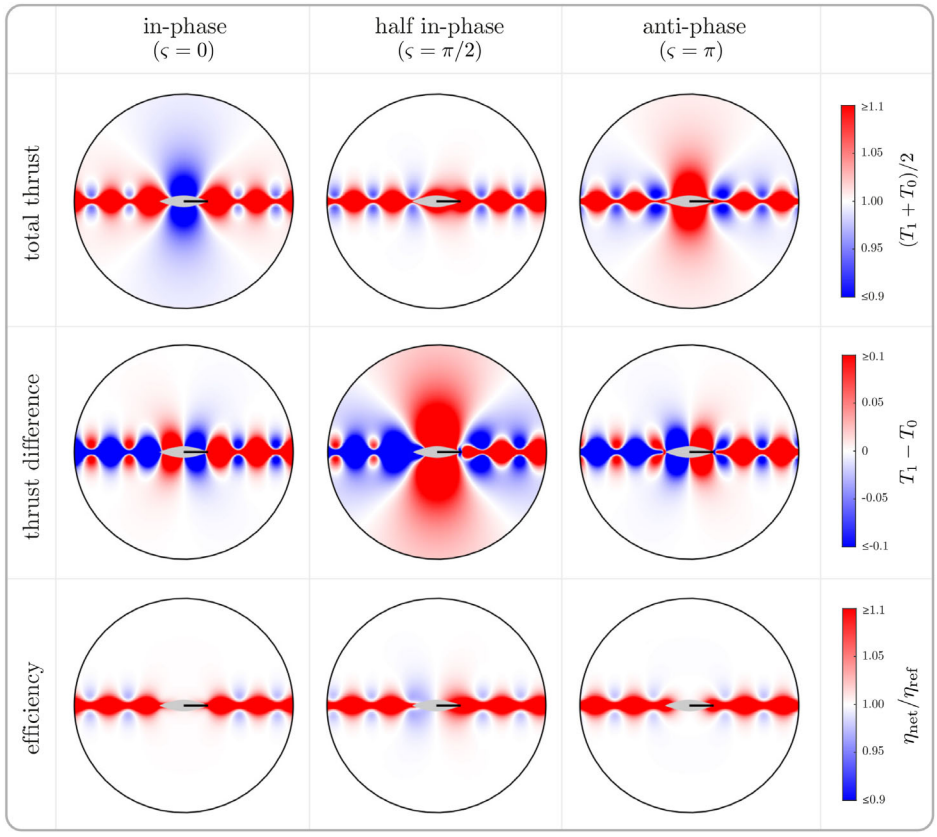

FIGURE 9 The dependence of dynamic quantities on the relative positions of a pair of pitching foils at $\sigma = 2$.

results from Figure 6a, and viewing the figure off axis generalizes those results. In particular, picking a point on the y-axis corresponds to a side-by-side configuration. For this arrangement, the $\varsigma = 0$ panel shows that in-phase heaving reduces the net thrust, while the $\varsigma = \pi$ panel shows that anti-phase heaving increases the net thrust. Both results are consistent with the physical intuition gained from the pressure fields in Figures 4b–5b. That is, in-phase heaving causes the fluid between the plates to move cohesively thereby reducing net thrust, whereas the squeezing effect of anti-phase heaving creates a high-pressure region in between which enhances net thrust.

The middle row of Figure 8 shows the difference in thrusts, $T_1 - T_0$, where T_0 corresponds to the foil at the origin and T_1 to the second foil located arbitrarily. Thus, red (blue) indicates that the second foil generates greater (less) thrust than the one located at the origin. Of particular importance are the zero-contours of $T_1 - T_0$, along which two free-swimmers generate equal thrust and would therefore maintain their relative positions. These contours generalize the predictions for inline equilibria (Section 5.2) to arbitrary arrangements not considered in previous models [50, 53].

Interestingly, this middle row shows several bounded contours of $T_1 - T_0 = 0$, and a handful of unbounded contours. The unbounded contours, in particular, imply that equilibrium configurations with arbitrarily large lateral separation are possible. That is, the swimmers do not necessarily need to be tightly clustered in order to achieve an equilibrium configuration. More specifically, for both in-phase ($\varsigma = 0$) and anti-phase ($\varsigma = \pi$) heaving, an unbounded contour extends

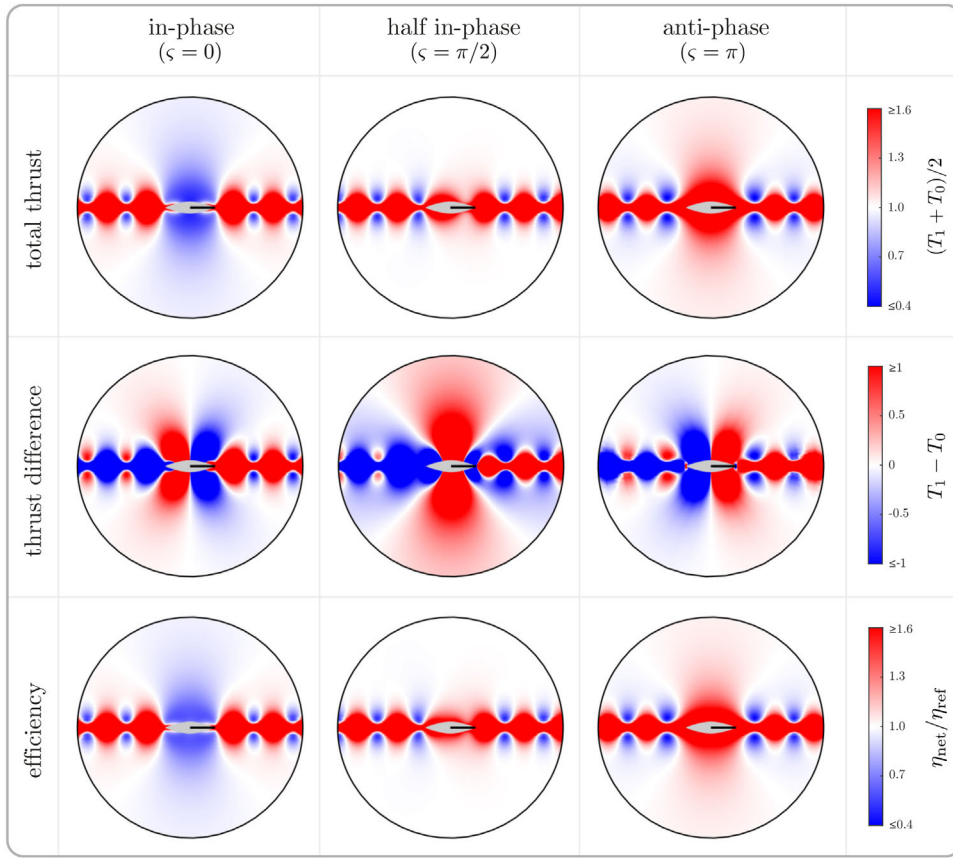

FIGURE 10 The dependence of dynamic quantities on the relative positions of a pair of waving foils at $\sigma = 2$.

vertically along the y-axis, indicating that the side-by-side configuration is an equilibrium. Moreover, examining the surrounding sign of $T_1 - T_0$ (i.e., red or blue on the figure) indicates this configuration to be stable to streamwise perturbations if the foils heave out of phase ($\varsigma = \pi$), and unstable if they heave in phase ($\varsigma = 0$).

Perhaps the most surprising results come from the case of a 90-degree phase offset in kinematics, ($\varsigma = \pi/2$). Here, the side-by-side arrangement is not an equilibrium, and instead the unbounded contours of $T_1 - T_0 = 0$ extend outwards at an angle. Hence, equilibrium is achieved by a staggered arrangement. By evaluating the sign of $T_1 - T_0$, we find the rightward-extending branches to be unstable and the leftward ones to be stable. The physical consequence is that the kinematic phase ς pre-selects the swimmer that will ultimately emerge as the positional leader. That is, the swimmer that leads in phase will ultimately lead the configuration, provided that the initial arrangement lies within the basin of attraction of the stable contour. Otherwise, the horizontal separation between the swimmers will grow indefinitely.

The bottom row of Figure 8 shows the net efficiency of the configuration,

$$\eta_{\text{net}} = \frac{U(T_0 + T_1)}{P_0 + P_1}, \tag{5.1}$$

normalized by the efficiency of a single swimmer performing the same motions (η_{ref}). This figure shows that, by and large, the swimming pair achieves the same (white) or slightly better (red) efficiency than a single swimmer. For the inline configurations (along the horizontal axis of the figure), the pair almost always enjoys higher efficiency. There are also smaller blue regions, where the efficiency of the pair suffers. Off of the horizontal axis, the average efficiency converges to the single-swimmer value (white) rather rapidly, indicating that thrust enhancements are typically accompanied by higher power requirements when the vertical distance between the swimmers is significant.

The panels of Figure 8 exhibit several symmetries. The up-down symmetry of each panel arises because, geometrically, $y_1 \mapsto -y_1$ is equivalent to $\{y,\ h_{0,1}\} \mapsto \{-y,\ -h_{0,1}\}$. Since the problem is linear, this transformation effects $\phi(z) \mapsto -\phi(\overline{z})$, and the sign changes in ϕ and $h_{0,1}$ ultimately cancel in the formulas for thrust (F.5, F.6) and power (F.7). For $\varsigma = 0, \pi$, the total thrust and net efficiency are left-right symmetric whereas the thrust difference is left-right skew-symmetric. To see why, note that, if $x_0^- = 0$, reflection in the y-axis ($x_1 \mapsto -x_1$) is equivalent to $\{y,\ h_{0,1}\} \mapsto \{-y,\ -h_{1,0}\}$. Thus, using the reasoning above and, since the kinematics are identical modulo a sign, this transformation swaps the thrust and power between the swimmers: $\{T_{0,1},\ P_{0,1}\} \mapsto \{T_{1,0},\ P_{1,0}\}$. As can be seen in Figure 8, this left-right symmetry is absent for $\varsigma = \pi/2$.

How are these results affected by the mode of locomotion? We briefly address this question in Figure 9 by showing analogous plots for *pitching* foils. The foils are pitching about their leading edges so the kinematics are given by $h_m(x,t) = (1/2)(x - x_m^-)\cos(2\pi t + m\varsigma)$. By comparing the figures to the corresponding plots for heaving kinematics, we observe that the average (top row) and difference (middle row) of thrusts have a qualitatively similar structure along the vertical midplane (y-axis). Specifically, the cases $\varsigma = 0$ and $\varsigma = \pi$ in both Figure 8 and Figure 9 show that the hydrodynamic thrust is relatively low for in-phase flapping and high for antiphase flapping. Moreover, the vertical contour of $T_1 - T_0 = 0$ indicates that the side-by-side arrangement is an equilibrium for both in-phase ($\varsigma = 0$) and anti-phase ($\varsigma = \pi$) pitching, as was also observed for heaving foils.

However, there are some notable differences between heaving and pitching kinematics. For inline configurations of heaving foils, the average thrust oscillates between values greater and less than unity as the distance from the leader is progressively increased (Figure 6 and Figure 8), but it is always greater than unity for pitching foils (Figure 9). Moreover, the middle row of Figure 9 suggests that for in-phase inline pitching foils, the follower always generates greater thrust and would thus tend to catch up to the leader. The zero-contour of $T_1 - T_0$ lies off axis and therefore an equilibrium arrangement requires the swimmers to be offset vertically. The same is nearly true when the follower has a nonzero phase offset, except for a small region near the trailing edge of the leader where the thrust difference is negative, which leads to a single (stable) equilibrium point for which the foils are nearly touching. We note that the presence of either zero ($\varsigma = 0$) or one ($\varsigma = \pi/2$ and π) in-line equilibrium configurations contrasts with the case of heaving kinematics (Figure 8), for which there exists a discrete set of equilibria along the horizontal midplane. Our predictions in the middle row of Figure 9 ($\varsigma = \pi$) are qualitatively consistent with recent experiments on pitching hydrofoils in a water tank with an imposed free stream flow [36], in which a single in-line equilibrium with closely-spaced foils was observed. We also show the net efficiency in the bottom row of Figure 9. Once again, the swimming pair generally operates at slightly higher (red) or the same (white) efficiency as does a single swimmer.

In addition to heaving and pitching, our theory can easily handle more intricate kinematics, such as the so-called waving motions originally studied in the single-body case by Wu [62]. To illustrate, Figure 10 shows thrust and efficiency values associated with the undulatory kinematics

$h_m(x,t) = (1/2)(x - x_m^-)\cos(2(x - x_m^- - 1) + 2\pi t + m\varsigma)$ where $m = 0$ represents the foil located at the origin and $m = 1$ the one located arbitrarily. The results for the average thrust (top row) are qualitatively similar to those for pitching foils for all phase differences considered. The results for the thrust difference (middle row) are also similar to the pitching case. The most salient difference is observed for antiphase kinematics, for which the zero-contour of $T_1 - T_0$ just downstream of the foil shown consists of a single connected component for the pitching configuration but three separate components for the undulatory kinematics.

Some of the physical results in this section have been corroborated by numerical simulations of the Navier–Stokes equations and experiments on pairs of flapping foils in a water tank. For the inline configuration, numerical [3, 14, 22, 48] and experimental [13, 30, 41, 53, 61] studies have found that the hydrodynamic thrust oscillates with the separation distance and/or the phase offset ς, as we observed in Figure 7b. Meanwhile, for the side-by-side configuration, Figures 8 and 9 (top left panels) show that in-phase oscillations lead to a decrease in the net thrust, as observed in experiments [23]. By contrast, Figures 8 and 9 (top right panels) show that anti-phase oscillations cause a dramatic increase in the thrust, a finding that has been observed in experiments [23] and simulations [12, 24]. Furthermore, for the case of anti-phase pitching (Figure 9, right panels), our prediction of a single stable inline equilibrium is consistent with recent experiments on pitching foils in a water tank [36].

6 | CONCLUSIONS

In this paper, we have generalized classical waving-plate theory to handle multiple swimming bodies. Our analysis relies on conformally mapping multiply-connected domains via the prime function, a special function whose application to varied physical problems has only recently been explored. In our theory, flow-mediated interactions between swimmers are handled directly via the acceleration potential (or pressure field), with vortex shedding accounted for by the singularity structure of the solution. Importantly, the analysis introduces no new ad-hoc assumptions regarding the separation distance between swimmers or the direction of influence (e.g., a leader/follower relationship), in contrast with other recently developed models.

For the case of two interacting swimmers, we have presented an efficient method for evaluating the solutions and compared against existing experimental results. The theory recovers a range of observed behaviors, including the dependence of thrust on swimmer configuration and relative phase, and the emergence of integer-valued "schooling modes" for free swimmers. Generally, Figure 7b suggests that the dominant physics of the interaction between inline heaving wings is controlled by the phasing between the follower's leading edge and the leader's wake. This physical picture is consistent with that proposed in 2D [42] and 3D [38] numerical simulations of pairs of swimming bodies with realistic fish-like kinematics.

We remark that most of the two-body effects mentioned above are traditionally thought of as wake-induced interactions, a perspective that we do not dispute. However, it is remarkable that our method accurately captures these effects *without ever explicitly resolving vortex wakes*. Wakes are certainly present in the model and accounted for by the singularity structure of the acceleration potential, but they do not need to be computed explicitly in order to determine the hydrodynamic forces on the swimmers. Rather, the pressure field serves as the intermediary.

Because our solutions are primarily analytical in nature, the numerical requirements are light (mainly evaluation of special functions and quadrature), which enables extremely efficient sweeps

through parameter space. Figure 8 for example contains roughly 21,000 solution evaluations, each one of which represents the simulated interaction between a pair of swimmers in a different configuration. The creation of this entire figure required roughly 5 min of CPU time, whereas other simulation methods might require significant resources to obtain just a handful of data points on this plot.

We have invested the effort in extending the waving-plate formulation of Wu to multiply-connected domains because we see distinct advantages in working with the acceleration potential, or pressure field, as the main state variable. First, unlike a velocity potential, the acceleration potential enjoys analyticity throughout the entire fluid domain, even crossing vortex-sheet wakes where the velocity potential suffers a discontinuity. This feature provides great mathematical convenience. Second, compared to a method that explicitly resolves vortex sheets (e.g., through solving integral equations), the pressure field offers a more direct description of hydrodynamic interactions. The vorticity formulation, while it remains an indispensable theoretical tool, introduces a few degrees of separation between the main state variable and the physics of interest. That is, once the vortex sheets are computed, the Biot–Savart law must be invoked to obtain the velocity field, and then the unsteady Bernoulli equation gives the pressure distribution, after which it is finally possible to calculate the hydrodynamic forces acting on each surface. This indirect path might call into the question the ability to draw meaningful conclusions regarding hydrodynamic interactions from visualizations of vorticity. The current approach, however, reframes the mathematical problem in terms of the pressure field, thus directly linking the primary state variable to the physics of interest.

At the same time, the newly developed theory is not without limitations. In particular, the flat structure of vortex wakes implied by the theory precludes discussion of more exotic phenomena, such as vortex sheet roll-up or wake deflection [12, 31, 37, 49], which may play a role in altering hydrodynamic forces under certain circumstances. It might be possible to extend the theory to higher order to capture such effects, and such an extension is a worthwhile endeavor for future investigations.

Lastly, since our theory does not constrain the relative location of the swimmers or their actuation, it offers a number of new predictions. One example is the off-axis equilibrium configurations anticipated by the middle rows of Figures 8–10 for heaving, pitching, and undulatory kinematics, respectively. Most previous laboratory experiments constrained the vertical positions of swimmers, and thus only observed the inline equilibria, but this constraint could be removed to search for staggered arrangements (e.g. [36]). For biological systems, the vertical constraint is completely artificial, so staggered arrangements should be just as likely to occur as inline ones. In a similar vein, our theory easily handles swimmers actuated at different frequencies (see Appendix A). Thoroughly exploring the range of new predictions and seeking corroboration from laboratory experiments is an exciting avenue for future work.

ACKNOWLEDGEMENTS

The authors would like to thank the Isaac Newton Institute for Mathematical Sciences for support and hospitality during the programme "Complex analysis: techniques, applications and computations" (supported by EPSRC grant no. EP/R014604/1) where the ideas for this paper were first generated. NJM thanks the NSF (grant no. DMS-2012560) and the Simons Foundation (grant no. 524259) for their support. AUO also acknowledges the support of the Simons Foundation (Collaboration Grant for Mathematicians, grant no. 587006) and NSF (grant no. DMS-2108839), and

his visit to the programme was partially supported by a travel award from the NSF (grant no. DMS-1933403).

ORCID

Peter J. Baddoo https://orcid.org/0000-0002-8671-6952
Nicholas J. Moore https://orcid.org/0000-0001-9578-7982
Anand U. Oza https://orcid.org/0000-0002-9079-9172
Darren G. Crowdy https://orcid.org/0000-0002-7162-0181

REFERENCES

1. ACCA Github page: SKPrime software, https://github.com/ACCA-Imperial.
2. M. J. Ablowitz and A. S. Fokas, *Complex Variables: Introduction and Applications*, vol. XXXIII, Cambridge University Press, 2003. 9809069v1. Available at: http://www.ncbi.nlm.nih.gov/pubmed/15003161%5Cnhttp://cid.oxfordjournals.org/lookup/doi/10.1093/cid/cir991%5Cnhttp://www.scielo.cl/pdf/udecada/v15n26/art06.pdf%5Cnhttp://www.scopus.com/inward/record.url?eid=2-s2.0-84861150233&partnerID=tZOtx3y1.
3. I. Akhtar, R. Mittal, G. V. Lauder, and E. Drucker, *Hydrodynamics of a biologically inspired tandem flapping foil configuration*, Theor. Comput. Fluid Dyn. **21** (2007), no. 3, 155–170.
4. J. Alaminos-Quesada and R. Fernandez-Feria, *Aerodynamics of heaving and pitching foils in tandem from linear potential theory*, AIAA J. **58** (2020), no. 1, 37–52.
5. J. Alaminos-Quesada and R. Fernandez-Feria, *Propulsion performance of tandem flapping foils with chordwise prescribed deflection from linear potential theory*, Phys. Rev. Fluids **6** (2021), no. 1, 013102.
6. S. Alben, *Simulating the dynamics of flexible bodies and vortex sheets*, J. Comput. Phys. **228** (2009), 2587–2603.
7. S. Alben, *Collective locomotion of two-dimensional lattices of flapping plates. Part 1. Numerical method, single-plate case and lattice input power*, J. Fluid Mech. **915** (2021), A20.
8. S. Alben, *Collective locomotion of two-dimensional lattices of flapping plates. Part 2. Lattice flows and propulsive efficiency*, J. Fluid Mech. **915** (2021), A21.
9. I. Ashraf, H. Bradshaw, T.-T. Ha, J. Halloy, R. Godoy-Diana, and B. Thiria, *Simple phalanx pattern leads to energy saving in cohesive fish schooling*, Proc. Natl. Acad. Sci. USA **114** (2017), no. 36, 9599–9604.
10. P. J. Baddoo, M. Kurt, L. J. Ayton, and K. W. Moored, *Exact solutions for ground effect*, J. Fluid Mech. Rapids **891** (2020), R2.
11. H. F. Baker, *Abelian functions: Abel's theorem and the allied theory of theta functions*, Cambridge University Press, 1897.
12. Y. Bao, D. Zhou, J. J. Tao, Z. Peng, H. B. Zhu, Z. L. Sun, and H. L. Tong, *Dynamic interference of two anti-phase flapping foils in side-by-side arrangement in an incompressible flow*, Phys. Fluids **29** (2017), no. 3, 033601.
13. B. M. Boschitsch, P. A. Dewey, and A. J. Smits, *Propulsive performance of unsteady tandem hydrofoils in an in-line configuration*, Phys. Fluids **26** (2014), no. 5, 051901.
14. T. M. Broering, and Y.-S. Lian, *The effect of phase angle and wing spacing on tandem flapping wings*, Acta Mech. Sin. **28** (2012), no. 6, 1557–1571.
15. D. G. Crowdy, *Calculating the lift on a finite stack of cylindrical aerofoils*, Proc. Roy. Soc. A. **462** (2006), 1387–1407.
16. D. G. Crowdy, *The Schwarz problem in multiply connected domains and the Schottky–Klein prime function*, Complex Var. Elliptic Equ. **53** (2008), no. 3, 221–236.
17. D. G. Crowdy, *A new calculus for two-dimensional vortex dynamics*, Theor. Comput. Fluid Dyn. **24** (2010), no. 1-4, 9–24.
18. D. G. Crowdy, *Solving problems in multiply connected domains*, SIAM CBMS-NSF Regional Conference Series in Applied Mathematics, 2020.
19. D. G. Crowdy, and V. S. Krishnamurthy, *The effect of core size on the speed of compressible hollow vortex streets*, J. Fluid Mech. **836** (2018), 797–827. Available at: https://doi.org/10.1017/jfm.2017.821.
20. D. G. Crowdy, E. H. Kropf, C. C. Green, and M. M. S. Nasser, *The Schottky-Klein prime function: A theoretical and computational tool for applications*, IMA J. Appl. Math. **81** (2016), no. 3, 589–628.

21. D. G. Crowdy and J. Marshall, *Conformal mappings between canonical multiply connected domains*, Comput. Methods Funct. Theory **6** (2006), no. 1, 59–76.
22. J. Deng, X.-M. Shao, and Z.-S. Yu, *Hydrodynamic studies on two traveling wavy foils in tandem arrangement*, Phys. Fluids **19** (2007), no. 11, 113104.
23. P. A. Dewey, D. B. Quinn, B. M. Boschitsch, and A. J. Smits, *Propulsive performance of unsteady tandem hydrofoils in a side-by-side configuration*, Phys. Fluids **26** (2014), no. 4, 041903.
24. G.-J. Dong and X.-Y. Lu, *Characteristics of flow over traveling wavy foils in a side-by-side arrangement*, Phys. Fluids **19** (2007), no. 5, 057107.
25. F. Fang, K. L. Ho, L. Ristroph, and M. J. Shelley, *A computational model of the flight dynamics and aerodynamics of a jellyfish-like flying machine*, J. Fluid Mech. **819** (2017), 621–655.
26. R. Fernandez-Feria, *Linearized propulsion theory of flapping airfoils revisited*, Phys. Rev. Fluids **1** (2016), no. 8, 084502.
27. I. E. Garrick, *Propulsion of a flapping and oscillating airfoil*, NACA **TR 567** (1936).
28. J. D. Geder, R. Ramamurti, D. Edwards, T. Young, and M. Pruessner, *Development of an unmanned hybrid vehicle using artificial pectoral fins*, Mar. Technol. Soc. J. **51** (2017), no. 5, 56–70.
29. R. Godoy-Diana, J. Vacher, V. Raspa, and B. Thiria, *On the fluid dynamical effects of synchronization in side-by-side swimmers*, Biomimetics **4** (2019), no. 4, 77.
30. W. Q. Gong, B. B. Jia, and G. Xi, *Experimental study on mean thrust of two plunging wings in tandem*, AIAA **53** (2015), no. 6, 1693–1705.
31. A. Gungor and A. Hemmati, *Wake symmetry impacts the performance of tandem hydrofoils during in-phase and out-of-phase oscillations differently*, Phys. Rev. E **102** (2020), no. 4, 043104.
32. J. Herskin and J. F. Steffensen, *Energy savings in sea bass swimming in a school: measurements of tail beat frequency and oxygen consumption at different swimming speeds*, J. Fish Biol. **53** (1998), 366–376.
33. A. P. Hoover, R. Cortez, E. D. Tytell, and L. J. Fauci, *Swimming performance, resonance and shape evolution in heaving flexible panels*, J. Fluid Mech. **847** (2018), 386–416.
34. Y. Huang, M. Nitsche, and E. Kanso, *Hovering in oscillatory flows*, J. Fluid Mech. **804** (2016), 531–549.
35. J. Katz and A. Plotkin, *Low-Speed Aerodynamics*, Cambridge University Press, Cambridge, 2009. arXiv:1011.1669v3. Available at: http://ebooks.cambridge.org/ref/id/CBO9780511810329http://link.springer.com/10.1007/978-1-4020-8664-9_3
36. M. Kurt, A. Mivehchi, and K. W. Moored, *Two-dimensionally stable self-organization arises in simple schooling swimmers through hydrodynamic interactions*, arXiv:2102.03571 (2021).
37. M. Kurt, A. E. Panah, and K. W. Moored, *Flow interactions between low aspect ratio hydrofoils in in-line and staggered arrangements*, Biomimetics **5** (2020), no. 2, 13.
38. G. Li, D. Kolomenskiy, H. Liu, B. Thiria, and R. Godoy-Diana, *On the energetics and stability of a minimal fish school*, PLoS ONE **14**(8) (2019), no. e0215265.
39. L. Li, M. Nagy, J. M. Graving, J. Bak-Coleman, G. Xie, and I. D. Couzin, *Vortex phase matching as a strategy for schooling in robots and in fish*, Nat. Comm. **11** (2020), no. 5408.
40. X. Lin, J. Wu, T. Zhang, and L. Yang, *Phase difference effect on collective locomotion of two tandem autopropelled flapping foils*, Phys. Rev. Fluids **4** (2019), no. 5, 054101.
41. K. B. Lua, X. H. Zhang, T. T. Lim, and K. S. Yeo, *Aerodynamics of two-dimensional flapping wings in tandem configuration*, Phys. Fluids **28** (2016), no. 12, 121901.
42. N. S. Lagopoulos, G. D. Weymouth, and B. Ganapathisubramani, *Deflected wake interaction of tandem flapping foils*, J. Fluid Mech. **903** (2020).
43. A. P. Maertens, A. Gao, and M. S. Triantafyllou, *Optimal undulatory swimming for a single fish-like body and for a pair of interacting swimmers*, J. Fluid Mech. **813** (2017), 301–345.
44. S. Marras, S. S. Killen, J. Lindström, D. J. McKenzie, J. F. Steffensen, and P. Domenici, *Fish swimming in schools save energy regardless of their spatial position*, Behav. Ecol. Sociobiol. **69** (2015), 219–226.
45. M. N. J. Moore, *Analytical results on the role of flexibility in flapping propulsion*, J. Fluid Mech. **757** (2014), 599–612.
46. M. N. J. Moore, *Torsional spring is the optimal flexibility arrangement for thrust production of a flapping wing*, Phys. Fluids **27** (2015), no. 9, 091 701.
47. M. N. J. Moore, *A fast Chebyshev method for simulating flexible-wing propulsion*, J. Comput. Phys. **345** (2017), 792–817.

48. T. J. Mueller and J. D. DeLaurier, *Aerodynamics of small vehicles*, Annu. Rev. Fluid Mech. **35** (2003), 89–111.
49. L. E. Muscutt, G. D. Weymouth, and B. Ganapathisubramani, *Performance augmentation mechanism of in-line tandem flapping foils*, J. Fluid Mech. **827** (2017), 484–505.
50. J. W. Newbolt, J. Zhang, and L. Ristroph, *Flow interactions between uncoordinated flapping swimmers give rise to group cohesion*, Proc. Natl. Acad. Sci. USA **116** (2019), no. 9, 2419–2424.
51. A. U. Oza, L. Ristroph, and M. J. Shelley, *Lattices of hydrodynamically interacting flapping swimmers*, Phys. Rev. X **9** (2019), 041 024. Available at: https://link.aps.org/doi/10.1103/PhysRevX.9.041024
52. B. L. Partridge, J. Johansson, and J. Kalish, *The structure of schools of giant bluefin tuna in Cape Cod Bay*, Environ. Biol. Fishes **9** (1983), no. 3–4, 253–262.
53. S. Ramananarivo, F. Fang, A. Oza, J. Zhang, and L. Ristroph, *Flow interactions lead to orderly formations of flapping wings in forward flight*, Phys. Rev. Fluids **1** (2016), no. 7, 071201(R).
54. V. Raspa, R. Godoy-Diana, and B. Thiria, *Topology-induced effect in biomimetic propulsive wakes*, J. Fluid Mech. **729** (2013), 377–387.
55. A. J. Smits, *Undulatory and oscillatory swimming*, J. Fluid Mech. **874** (2019).
56. T. Theodorsen, *General theory of aerodynamic instability and the mechanism of flutter*, NACA **TR 496** (1935).
57. L. N. Trefethen and J. A. C. Weideman, *The Exponentially Convergent Trapezoidal Rule*, SIAM Rev. **56** (2014), no. 3, 385–458. Available at: http://129.67.184.129/trefethen/sirev56-3_385.pdf.
58. M. S. Triantafyllou, G. S. Triantafyllou, and D. K. P. Yue, *Hydrodynamics of fishlike swimming*, Annu. Rev. Fluid Mech. **32** (2000), 33–53.
59. T. von Kármán and J. M. Burgers, *General aerodynamic theory: Perfect fluids*, in Aerodynamic Theory, W. F. Durand (ed.), Sec. V.A.9, Springer, Berlin, 1935, pp. Vol II.
60. T. von Kármán and W. R. Sears, *Airfoil theory for non-uniform motion*, J. Aeronaut. Sci. **5** (1938), no. 10, 379–390.
61. J. Warkentin and J. DeLaurier, *Experimental aerodynamic study of tandem flapping membrane wings*, J. Aircraft **44** (2007), no. 5, 1653–1661.
62. T. Y. Wu, *Swimming of a waving plate*, J. Fluid Mech. **10** (1961), no. 03, 321–344.
63. T. Y. Wu, *Hydromechanics of swimming propulsion. Part 1. Swimming of a two-dimensional flexible plate at variable forward speeds in an inviscid fluid*, J. Fluid Mech. **46** (1971), no. 2, 337–355.
64. T. Y. Wu and A. T. Chwang, *Extraction of flow energy by fish and birds in a wavy stream*, in Swimming and flying in nature, Springer, 1975, pp. 687–702.

APPENDIX A: GENERAL HARMONIC MOTIONS

The calculations presented in the main text may readily be generalized to the case of plates flapping with different frequencies. Suppose that the m-th plate executes motions with frequency ω_m of the form

$$h_m(x,t) = h_m^c(x)\cos(\omega_m t) + h_m^s(x)\sin(\omega_m t). \tag{A.1}$$

There will be a subset $\{\tilde{\omega}_m\} \subseteq \{\omega_m\}$ of $\tilde{M}$ distinct frequencies. Since the problem is linear, the acceleration potential and velocity fields will be composed of linear responses to these distinct frequencies:

$$f(z,t) = \sum_{m=0}^{\tilde{M}} [f_m^c(z)\cos(\tilde{\omega}_m t) + f_m^s(z)\sin(\tilde{\omega}_m t)], \tag{A.2}$$

$$w(z,t) = \sum_{m=0}^{\tilde{M}} [w_m^c(z)\cos(\tilde{\omega}_m t) + w_m^s(z)\sin(\tilde{\omega}_m t)]. \tag{A.3}$$

We therefore introduce the vectorized quantities

$$\boldsymbol{f}(z) = \begin{bmatrix} f_0^c(z) & f_0^s(z) & \cdots & f_{\tilde{M}}^c(z) & f_{\tilde{M}}^s(z) \end{bmatrix}^T, \tag{A.4}$$

$$\boldsymbol{w}(z) = \begin{bmatrix} w_0^c(z) & w_0^s(z) & \cdots & w_{\tilde{M}}^c(z) & w_{\tilde{M}}^s(z) \end{bmatrix}^T. \tag{A.5}$$

In this notation, (2.4) becomes

$$\partial_z \boldsymbol{f}(z) = \boldsymbol{V}\boldsymbol{w}(z) + U\partial_z \boldsymbol{w}(z) \tag{A.6}$$

where $\boldsymbol{V} \in \mathbb{R}^{2\tilde{M}\times 2\tilde{M}}$ is a block diagonal matrix:

$$\boldsymbol{V} = \begin{bmatrix} \tilde{\omega}_0 \boldsymbol{J} & & \boldsymbol{0} \\ & \ddots & \\ \boldsymbol{0} & & \tilde{\omega}_{\tilde{M}} \boldsymbol{J} \end{bmatrix} = \operatorname{diag}\left(\begin{bmatrix} \tilde{\omega}_0 \boldsymbol{J} & \tilde{\omega}_1 \boldsymbol{J} & \cdots & \tilde{\omega}_{\tilde{M}} \boldsymbol{J} \end{bmatrix} \right). \tag{A.7}$$

Equation (A.6) can be inverted to obtain

$$\boldsymbol{w}(z) = \frac{1}{U} \mathrm{e}^{-\boldsymbol{\Sigma} z} \int_{-\infty}^{z} \mathrm{e}^{\boldsymbol{\Sigma} z'} \partial_z \boldsymbol{f}(z') \mathrm{d}z' \tag{A.8}$$

where $\boldsymbol{\Sigma} = \boldsymbol{V}/U$. Since the exponential of a block diagonal matrix is the diagonal of the exponential of the blocks, we have $\mathrm{e}^{\boldsymbol{\Sigma} z} = \operatorname{diag}\left(\begin{bmatrix} \mathrm{e}^{\sigma_0 \boldsymbol{J}} & \cdots & \mathrm{e}^{\sigma_{\tilde{M}} \boldsymbol{J}} \end{bmatrix} \right)$ where $\sigma_k = \tilde{\omega}_k / U$. Now, all the other calculations of the paper follow with $\sigma \boldsymbol{J}$ replaced with $\boldsymbol{\Sigma}$.

Another perspective is that the motion of each plate can be represented as a superposition of contributions from all frequencies in the system. For example, consider two plates flapping with frequencies ω_0 and ω_1, respectively. Then, the problem is equivalent to solving two problems, each of which consists of a single plate flapping with a particular frequency (ω_0 or ω_1) while the other plate is stationary.

APPENDIX B: COMPARISON TO WU'S SOLUTION

Here we show that our single plate solution in Section 2.2 is equivalent to that derived by Wu [62].

In the single plate case ($M = 0$), the canonical circular domain is the unit disc and the mapping is the Joukowski map: $\mathcal{Z}(\zeta) = (\zeta + \zeta^{-1})/2$. The associated prime function is simply $\omega(\zeta, \alpha) = \zeta - \alpha$. Wu's solution is expressed in the circular domain as the Laurent series

$$L(\zeta) = \mathrm{i}U^2 \sum_{n=1}^{\infty} a_n \zeta^n \tag{B.1}$$

where the coefficients a_n are given by the recurrence relation

$$a_n = \lambda_n + \frac{j\sigma}{2n}(\lambda_{n-1} - \lambda_{n+1}). \tag{B.2}$$

The λ_n are the coefficients of the Chebyshev expansion of the material derivative of the plate motion:

$$(j\sigma + \partial_x) h_0(x) = -\frac{\lambda_0}{2} - \sum_{n=1}^{\infty} \lambda_n T_n(x), \tag{B.3}$$

where T_n denotes the Chebyshev polynomials of the first kind. Applying the orthogonality property of Chebyshev polynomials yields

$$\lambda_n = \frac{-2}{\pi}\int_{-1}^{1}\frac{T_n(x)}{\sqrt{1-x^2}}(j\sigma + \partial_x)h_0(x)\mathrm{d}x.$$

As discussed in Section 2.1, Wu uses the complex 'j' notation where the real part of the solution is assumed with respect to the imaginary unit j. For ease of comparison, we also adopt this notation in this section. Wu also treats h_0 and $\partial_x h_0$ with similar Chebyshev expansions:

$$h_0(x) = \frac{\beta_0}{2} + \sum_{n=1}^{\infty}\beta_n T_n(x), \qquad \partial_x h_0(x) = \frac{\gamma_0}{2} + \sum_{n=1}^{\infty}\gamma_n T_n(x) \tag{B.4}$$

so that $\lambda_n = -(\gamma_n + j\sigma\beta_n)$. The coefficients γ_n and β_n are connected by the recurrence relation $\gamma_{n-1} - \gamma_{n+1} = 2n\beta_n$ for $n > 0$.

To achieve correspondence with Wu's solution, we also expand our boundary data (2.7) in Chebyshev polynomials. The integral formula

$$\int^{x} T_n(x')\mathrm{d}x' = \begin{cases} T_1(x), & n = 0, \\ \frac{1}{4}T_2(x), & n = 1, \\ \frac{1}{2}\left(\frac{T_{n+1}(x)}{n+1} - \frac{T_{n-1}(x)}{n-1}\right), & n > 1, \end{cases} \tag{B.5}$$

allows us to write

$$\begin{aligned}\Psi_0(\zeta(x)) =& \text{const.} - U^2\left[\sum_{n=1}^{\infty}(\gamma_n + 2j\sigma\beta_n)T_n(x)\right. \\ &\left. -\sigma^2\frac{\beta_0}{2}T_1(x) - \sigma^2\frac{\beta_1}{4}T_2(x) - \frac{\sigma^2}{2}\sum_{n=2}^{\infty}\beta_n\left(\frac{T_{n+1}(x)}{n+1} - \frac{T_{n-1}(x)}{n-1}\right)\right].\end{aligned} \tag{B.6}$$

Expanding the first bracketed term and rearranging the term on the second line yields

$$\Psi_0(\zeta(x)) = \text{const.} + U^2\sum_{n=1}^{\infty}\left(\lambda_n - j\sigma\beta_n + \frac{\sigma^2}{2n}(\beta_{n-1} - \beta_{n+1})\right)T_n(x). \tag{B.7}$$

Finally, one can show that the bracketed term above is simply equal to a_n, so,

$$\Psi_0(\zeta(x)) = U^2\sum_{n=1}^{\infty}a_n T_n(x), \tag{B.8}$$

where we have set the constant of integration to be zero without loss of generality.

We may now insert the Chebyshev expansion (B.8) into the Poisson integral formula (2.24) to verify that we obtain the same regular solution (B.1) as Wu. Since $|\zeta| < 1$, (2.24) may be written as

$$L(\zeta) = \text{const.} + \sum_{n=1}^{\infty}\frac{\zeta^n}{\pi}\oint_{C_0}\Psi_0(\zeta')\frac{\mathrm{d}\zeta'}{(\zeta')^{n+1}}, \tag{B.9}$$

where we have interchanged the order of summation and integration. The constant term in (B.9) is purely imaginary and may thus be ignored. For the Joukowski map (2.19), $x = \cos\vartheta = \mathcal{Z}(e^{i\vartheta})$, so substituting (B.8) into (B.9) and using $T_k(\cos(\vartheta)) = \cos(k\vartheta)$ produces

$$L(\zeta) = \frac{U^2 \mathrm{i}}{\pi} \sum_{n=1}^{\infty} \zeta^n \sum_{k=1}^{\infty} a_k \int_0^{2\pi} \cos(k\vartheta) e^{-in\vartheta} \mathrm{d}\vartheta. \tag{B.10}$$

The remaining integral equals $\pi\delta_{k,n}$ so we finally have

$$L(\zeta) = \mathrm{i}U^2 \sum_{n=1}^{\infty} a_n \zeta^n \tag{B.11}$$

which is identical to the regular part of Wu's solution (B.1).

The singular part of Wu's solution is also recovered by our analysis. Detailing every step would involve tedious algebra so we will only provide an overview of the main steps. In particular, we will explicate how Bessel functions and the celebrated Theodorsen function arise. Wu expresses the singular part of the pressure field as

$$\frac{\mathrm{i}U^2 a_0}{\zeta + 1} \tag{B.12}$$

which, in the notation of the present paper, is

$$a_0 U^2 \hat{\mathcal{K}}(\zeta, \zeta_0^-) \tag{B.13}$$

where $\zeta_0^- = -1$ is the preimage of the leading edge. In the simply connected case, the integrals in Section 4.3 can be computed analytically in terms of Bessel functions so an analytical formula for a_0 can be found. The integral for the matrix $\boldsymbol{D}$ given in (4.9), which has just a single entry, becomes

$$U^2 D = -U \mathrm{Im}_{\mathrm{i}} \left[\int_{-\infty}^{z_0} e^{\sigma j (z - z_0)} \frac{\mathrm{d}}{\mathrm{d}z} \left(\frac{\mathrm{i}}{\zeta(z) + 1} \right) \mathrm{d}z \right] \tag{B.14}$$

where z_0 is an arbitrary point on the plate, and we are using Im_{i} to represent the imaginary part with respect to i specifically. Applying integration by parts then yields

$$U^2 D = -U \mathrm{Im}_{\mathrm{i}} \left[\frac{\mathrm{i}}{\zeta(z_0) + 1} - \sigma \mathrm{i} j \int_{-\infty}^{z_0} \frac{e^{\sigma j (z - z_0)}}{\zeta(z) + 1} \mathrm{d}z \right]. \tag{B.15}$$

The remaining integral can be expressed using Bessel functions: by inverting the Joukowski map (2.19), we obtain

$$\frac{1}{\zeta(z) + 1} = \frac{1}{1 + z + \sqrt{z^2 - 1}} = \frac{1}{2} \left(\frac{\mathrm{d}}{\mathrm{d}z} \left(z - \sqrt{z^2 - 1} \right) - \frac{1}{\sqrt{z^2 - 1}} \right). \tag{B.16}$$

On the other hand, the modified Bessel functions of the first kind can be expressed as

$$K_0(j\sigma) = \int_{-\infty}^{-1} \frac{e^{j\sigma z}}{\sqrt{z^2 - 1}} \mathrm{d}z, \qquad K_1(j\sigma) = j\sigma \int_{-\infty}^{-1} e^{j\sigma z} \sqrt{z^2 - 1}\, \mathrm{d}z. \tag{B.17}$$

Thus, choosing the integration endpoint as $z_0 = -1 + \epsilon \mathrm{i}$, applying (B.16) and (B.17) and taking the limit $\epsilon \to 0$ generates

$$\sigma j \int_{-\infty}^{z_0} \frac{\mathrm{e}^{j\sigma(z-z_0)}}{\zeta(z)+1} \mathrm{d}z = \frac{1}{2}\left[1 - j\sigma \mathrm{e}^{j\sigma}(K_1(j\sigma) + K_0(j\sigma))\right]. \tag{B.18}$$

Substituting (B.18) into (B.15) yields

$$U^2 D = -j\sigma U(K_1(j\sigma) + K_0(j\sigma)). \tag{B.19}$$

While we do not go into the details, similar arguments can be applied to express the integral (4.6) in terms of Bessel functions. Thus all the terms in the linear system (4.7) – which here is just a single complex scalar equation – can be expressed purely in terms of the motion of the plate and these Bessel functions. Solving this scalar equation yields

$$a_0 = (\lambda_0 + \lambda_1)C(\sigma) - \lambda_1$$

where

$$C(\sigma) = \frac{K_1(j\sigma)}{K_1(j\sigma) + K_0(j\sigma)}$$

is the Theodorsen function. Thus, our solution in Section 2.2 is identical to that derived by Wu [62].

APPENDIX C: DEGREES OF FREEDOM IN THE MAP

It is worth pointing out that the number of parameters matches the number of constraints in the map $\mathcal{Z}(\zeta)$ specified by (3.13). In the physical domain, there are $3(M+1)$ constraints, since each of the $M+1$ slits is determined by three parameters: two for position and one for length. As for the parameters, in the circular domain there are three parameters for each of the M excised circles: two for position and one for radius. Additionally, the complex parameters A, B and β contribute two further parameters each. There are three real degrees of freedom (two for translation and one for rotation) available in the Riemann Mapping Theorem. We insist that A is real, which fixes one of these. In general, we can pick β as we like, which fixes the other two. As such, there are $3M + 2 + 2 + 2 - 3 = 3(M+1)$ parameters remaining, which matches the number of constraints. We note that, for the two-plate case (Section 4.4), we instead fixed $\delta_1 = 0$ for the convenience of D_ζ being a concentric annulus, and had to find β.

APPENDIX D: EXPLICIT EXPRESSIONS FOR THE REGULAR PART OF THE SOLUTION

In certain simple situations it is possible to write down explicit solutions to the regular part of the solution $\boldsymbol{L}(\zeta)$ without using the integral formula (4.3). For example, the motion of $(M+1)$ plates executing identical, in-phase heaving motions may be described by

$$h_m^c(x) = h, \quad h_m^s(x) = 0, \qquad m = 0, \ldots, M. \tag{D.1}$$

Thus, the sine contribution L_s to the regular part is zero, whereas the cosine contribution L_c depends on h. L_c solves the boundary value problem (4.2), where the streamfunction takes values

$$\Psi_m^c(\zeta) = 4\pi^2 h x(\zeta). \tag{D.2}$$

To determine L_c we must find a function that is analytic in D_ζ and takes imaginary part equal to $4\pi^2 hx$ on the boundary as specified by (4.2). Since the boundaries in the physical domain are horizontal slits, the conformal map satisfies $\mathrm{Im}[\mathrm{i}\mathcal{Z}(\zeta)] = x(\zeta)$ when $\zeta \in \partial D_\zeta$. An ansatz for the regular solution is thus

$$L_c(\zeta) = 4\pi^2 \mathrm{i} h \mathcal{Z}(\zeta). \tag{D.3}$$

The ansatz (D.3) satisfies the boundary data specified by (4.2). However, this ansatz is not a valid solution to the boundary value problem because it is not analytic everywhere, since $\mathcal{Z}(\zeta)$ has a simple pole at $\zeta = \beta$. In particular,

$$L_c(\zeta) \sim \frac{4A\pi^2 \mathrm{i} h}{\zeta - \beta} \qquad \text{as} \quad \zeta \to \beta. \tag{D.4}$$

Hence, to obtain a valid solution to the boundary value problem we must remove the pole of the ansatz (D.3) without disturbing the imaginary part on the boundary ∂D_ζ. To achieve this, we combine the ansatz (D.3) with a function that has a simple pole of the correct magnitude and constant imaginary part on the boundaries (different constants on different boundaries). Crowdy [17] showed that

$$\mathcal{U}(\zeta) = -\mathrm{i}\left(\frac{1}{\beta} \mathcal{K}\left(\zeta, 1/\overline{\beta}\right) + \frac{1}{\beta} \mathcal{K}(\zeta, \beta) \right)$$

takes constant imaginary values on ∂D_ζ and

$$\mathcal{U}(\zeta) \sim \frac{\mathrm{i}}{\zeta - \beta} \qquad \text{as} \quad \zeta \to \beta.$$

Thus, the new ansatz $L_c(\zeta) = 4\pi^2 h(\mathrm{i}\mathcal{Z}(\zeta) - A\mathcal{U}(\zeta))$ takes the correct boundary values and is analytic in D_ζ. Expanding $\mathcal{Z}$ and $\mathcal{U}$ then gives

$$L_c(\zeta) = 8\pi^2 \mathrm{i} h \frac{A}{\beta} \mathcal{K}(\zeta, 1/\overline{\beta}). \tag{D.5}$$

The above expression is the regular part of the acceleration potential for any number of plates in any configuration provided that they are heaving with the same amplitude and phase. Similar expressions for pitching motions can be derived, though the algebra becomes quite complicated.

APPENDIX E: FAST COMPUTATION OF INTEGRALS COMPRISING THE SINGULAR PART OF THE SOLUTION

We present a computationally efficient method for evaluating the integrals that determine the unknown coefficients a_m in the singular part of the solution (Section 4.3). The integrals to be computed in (4.4) generally take the form

$$\int_{-\infty}^{z_m} \mathrm{e}^{\sigma \boldsymbol{J}(z - z_m)} \frac{\mathrm{d}\boldsymbol{r}}{\mathrm{d}z} \, \mathrm{d}z \tag{E.1}$$

for some vectorized function $\boldsymbol{r}$ whose components are analytic in D_z. Additionally, the components of $\boldsymbol{r}$ are bounded as $|z| \to \infty$. Recalling the expression (2.16) for $\mathrm{e}^{\sigma \boldsymbol{J} z}$ means that to compute

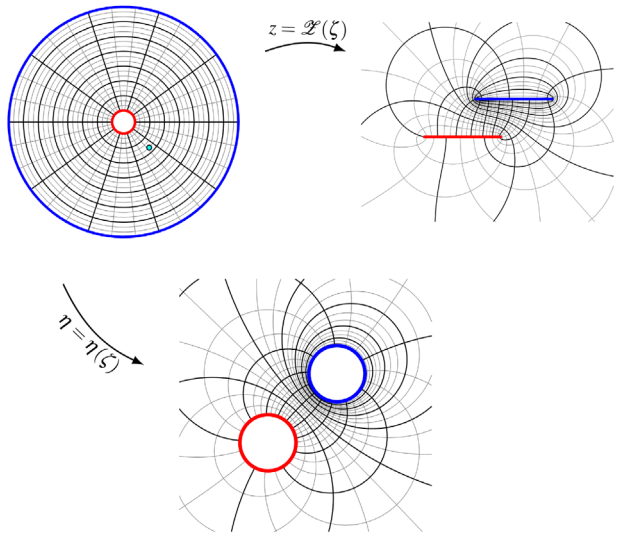

FIGURE E.1 Illustration of the mappings between D_ζ (top left), D_z (top right) and D_η (bottom).

(E.1) it is sufficient to compute

$$I^{\pm} = \int_{-\infty}^{z_m} \mathrm{e}^{\pm \mathrm{i}\sigma(z-z_m)} \frac{\mathrm{d}r}{\mathrm{d}z}\, \mathrm{d}z \tag{E.2}$$

where r is any component of $\boldsymbol{r}$. However, an expression for $r(z)$ is not readily available, so we rewrite the integral in D_ζ:

$$I^{\pm} = \int_{\beta^-}^{\zeta_m} \exp\left[\pm \mathrm{i}\sigma(\mathcal{Z}(\zeta) - z_m)\right] \frac{\mathrm{d}R}{\mathrm{d}\zeta}(\zeta)\mathrm{d}\zeta, \tag{E.3}$$

where $R(\zeta) = r(z)$ and β^- is the preimage of $-\infty$, that is, $\mathcal{Z}(\beta^-) = -\infty$.

By (3.13), we can express the conformal map as

$$\mathcal{Z}(\zeta) = \frac{A}{\zeta - \beta} + \tilde{\mathcal{Z}}(\zeta), \tag{E.4}$$

where $\tilde{\mathcal{Z}}$ is analytic in D_ζ and finite at β. The residue of $\mathcal{Z}$ at β is given by $A \in \mathbb{R}$. There is an essential singularity at $\zeta = \beta$ and we cannot integrate through this singularity.

We now introduce the substitution

$$\eta(\zeta) = \frac{\zeta_m - \zeta}{\zeta - \beta} \cdot \frac{1}{\zeta_m - \beta}, \qquad \zeta(\eta) = \frac{\eta\beta(\beta - \zeta_m) - \zeta_m}{(\beta - \zeta_m)\eta - 1}, \tag{E.5}$$

where ζ_m is the pre-image of the endpoint of the integral: $z_m = \mathcal{Z}(\zeta_m)$. This is a Möbius map so the boundary circles are mapped to boundary circles. Note that the point $\zeta = \beta^-$ is mapped to $\eta = -\infty$, so D_η is exterior to the boundary circles. This domain is similar to the initial physical domain, except the flat plate boundaries are now circles; the arrangement is illustrated in Figure E.1.

The exponential term in the integrals can now be manipulated using (E.4) into a form amenable to Gauss–Laguerre quadrature:

$$\exp\left[\pm i\sigma(\mathcal{Z}(\zeta)-z_m)\right]=\exp\left[\pm i\sigma A\eta\right]\exp\left[\pm i\sigma\left(\tilde{\mathcal{Z}}(\zeta(\eta))+\frac{A}{\zeta_m-\beta}-\mathcal{Z}(\zeta_m)\right)\right]. \tag{E.6}$$

The integrals (E.3) may thus be written in D_η:

$$\begin{aligned} I^{\pm} =& \exp\left[\pm i\sigma\left(\frac{A}{\zeta_m-\beta}-\mathcal{Z}(\zeta_m)\right)\right] \\ &\times\int_{-\infty}^{0}\exp\left[\pm i\sigma A\eta\right]\exp\left[\pm i\sigma\tilde{\mathcal{Z}}(\zeta(\eta))\right]\frac{d\zeta}{d\eta}(\eta)\frac{dR}{d\zeta}(\zeta(\eta))d\eta. \end{aligned} \tag{E.7}$$

Also, note that

$$\frac{d\zeta}{d\eta}(\eta)=-\frac{(\zeta_m-\beta)^2}{\left((\zeta_m-\beta)\eta+1\right)^2}=\mathcal{O}\left(\frac{1}{\eta^2}\right)\qquad\text{as}\quad|\eta|\to\infty. \tag{E.8}$$

Since $dR/d\zeta(\beta)$ and $\tilde{\mathcal{Z}}(\beta)$ are bounded, the integrand of $I^{\pm}$ decays like $o(1/\eta)$ for $\mathrm{Im}(\eta)\gtrless 0$, so the limit of integration of $I^{\pm}$ can be deformed to $\pm i\infty$:

$$\begin{aligned} I^{\pm} =& -\exp\left[\pm i\sigma\left(\frac{A}{\zeta_m-\beta}-\mathcal{Z}(\zeta_m)\right)\right] \\ &\times\int_{0}^{\pm i\infty}\exp\left[\pm i\sigma A\eta\right]\exp\left[i\sigma\tilde{\mathcal{Z}}(\zeta(\eta))\right]\frac{d\zeta}{d\eta}(\eta)\frac{dR}{d\zeta}(\zeta(\eta))d\eta. \end{aligned} \tag{E.9}$$

The advantage of this approach is that the oscillatory exponential term is now a decaying exponential term. Now the integrand decays rapidly as $\eta\to\mathrm{sign}(A)\times i\infty$ and can be evaluated with a Gauss–Laguerre quadrature rule.

It is important to ensure that this contour deformation does not cross any poles, or their residue contribution should be included. For example, R could have a simple pole at the pre-image of the leading edge, and the new contour should not enclose this point in D_η. Some typical contour deformations are illustrated in Figure E.2. If $A>0$, then the contour for I^+ should be deformed into the upper half-plane (as indicated by the green contours), and the contour for I^- into the lower half-plane (purple contours). If $A<0$, then the contours for $I^{\pm}$ should be deformed into the lower/upper half-plane.

The deformed contour typically must include a circular arc section to ensure that it does not pass through any circles, since the integrand is not defined inside the circles. For example, in Figure E.2a there is a circular arc integral around part of the blue circle. Additionally, sometimes the deformed contour encloses a boundary circle, as in Figure E.2b. In this case, the residue around the enclosed circle must also be included. The specific choice of contour deformation described here is not unique, but experience suggests that it is the simplest to implement and automate when studying a large number of configurations, as we do in Section 5.

APPENDIX F: EXPRESSIONS FOR PHYSICAL QUANTITIES

Here we present expressions for the lift, thrust, and power for each foil along with the net efficiency and kinetic energy transfer of the full system. The expressions for the thrust, power, and

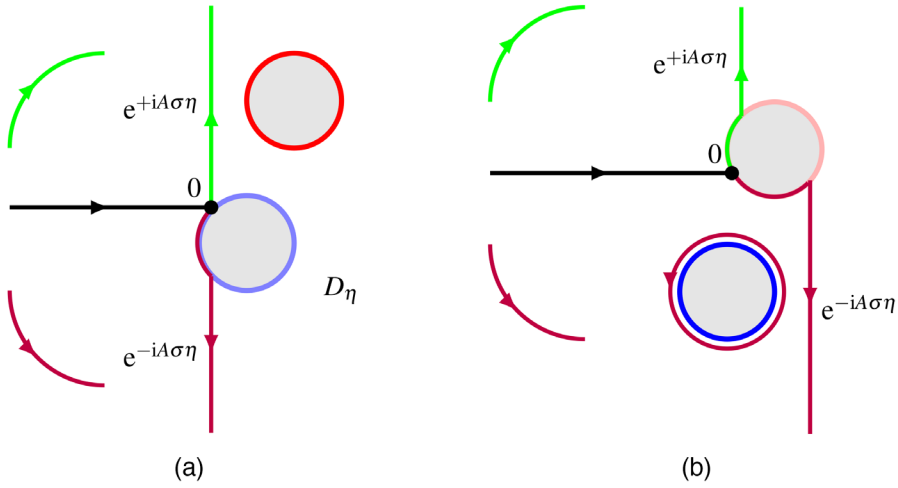

FIGURE E.2 An example of the deformed contours for $A > 0$. The black contour can be deformed to the green contour (for I^+) or the red contour (for I^-). In case (a) the endpoint is on the blue circle whereas in case (b) the endpoint is on the red circle.

efficiency were used to produce the figures in Section 5.2 and Section 5.3. While they are not used explicitly in the paper, we also record the expressions for the lift and kinetic energy transfer for the sake of completeness.

Our expressions are for nondimensional variables. Per unit span, the dimensional lift, thrust, power and kinetic energy transfer are connected to their dimensionless counterparts by

$$L = \frac{8\tilde{L}}{\rho c^3 f_d^2}, \qquad T = \frac{8\tilde{T}}{\rho c^3 f_d^2}, \qquad P = \frac{16\tilde{P}}{\rho c^4 f_d^3}, \qquad E = \frac{16\tilde{E}}{\rho c^4 f_d^3},$$

where tildes represent the corresponding dimensional quantity. The net propulsive efficiency (Section F.4) is non-dimensional by construction.

F.1 | Lift

The instantaneous lift exerted on each plate by the fluid is

$$L_m(t) = -\int_{x_m^-}^{x_m^+} \Delta\phi_m(x,t)\mathrm{d}x$$

where $\Delta\phi_m$ is the jump in acceleration potential across the m-th plate. Transforming the integral into D_ζ yields

$$L_m(t) = -\mathcal{X}_m \oint_{C_m} \phi(\zeta,t)\frac{\mathrm{d}\mathcal{Z}}{\mathrm{d}\zeta}(\zeta)\mathrm{d}\zeta, \tag{F.1}$$

where

$$\mathcal{X}_m = \begin{cases} -1 & \text{for} \quad m = 0, \\ +1 & \text{for} \quad m \neq 0 \end{cases}$$

accounts for the change in orientation when integrating around C_0. Analytical expressions for the lift force can be derived by applying the residue theorem to (F.1). However, we find this approach unwieldy and instead recommend evaluating the integrals using the trapezoidal rule, which converges exponentially fast in this context [57].

F.2 | Thrust

The instantaneous thrust on the m-th plate may be decomposed as

$$T_m(t) = T_m^{(p)}(t) + T_m^{(l)}(t) \tag{F.2}$$

where

$$T_m^{(p)}(t) = -\int_{z_m^-}^{z_m^+} \Delta\phi_m(x,t)\frac{\partial h_m}{\partial x}(x,t)\mathrm{d}x$$

is the contribution to the thrust from the pressure jump across the plate and $T_m^{(l)}$ is the leading-edge suction force. Again, $T_m^{(p)}$ can be transformed into D_ζ as

$$T_m^{(p)}(t) = -\mathcal{X}_m \oint_{C_m} \phi(\zeta,t)\frac{\partial h_m}{\partial x}(x(\zeta),t)\frac{\mathrm{d}\mathcal{Z}}{\mathrm{d}\zeta}(\zeta)\mathrm{d}\zeta.$$

The leading-edge suction forces $T_m^{(l)}$ are obtained by considering the dominant terms in the Bernoulli equation near the leading edge. Since the unsteady velocity potential and its time derivative are bounded, the dominant contribution comes from the quadratic interaction of the singular velocity. (Further details of this argument can be found on page 328 of [62].) Thus, the leading-edge suction force is

$$T_m^{(l)}(t) = \frac{\mathrm{i}}{2}\oint_{\mathcal{B}_m} w(z,t)^2\mathrm{d}z \tag{F.3}$$

where $\mathcal{B}_m$ is an ϵ-circle centered at z_m^-.

Transforming the integral into D_ζ produces

$$T_m^{(l)}(t) = \frac{\mathrm{i}}{2}\mathcal{X}_m \oint_{S_m} w(\mathcal{Z}(\zeta),t)^2\frac{\mathrm{d}\mathcal{Z}}{\mathrm{d}\zeta}(\zeta)\mathrm{d}\zeta \tag{F.4}$$

where S_m is an epsilon-semicircle centered at ζ_m^-. Since the image of each boundary circle is a horizontal slit, the derivative of the mapping function has the Taylor expansion $\frac{\mathrm{d}\mathcal{Z}}{\mathrm{d}\zeta}(\zeta) \sim (\zeta-\zeta_m^-)\frac{\mathrm{d}^2\mathcal{Z}}{\mathrm{d}\zeta^2}(\zeta_m^-)$ at ζ_m^-. Additionally, by (2.4) we have $w(\mathcal{Z}(\zeta),t) \sim UF(\zeta,t)$. Combining these behaviors with (3.9), (3.22) and (4.1) indicates that the integrand in (F.4) has a simple pole of the form

$$w(\mathcal{Z}(\zeta),t)^2\frac{\mathrm{d}\mathcal{Z}}{\mathrm{d}\zeta}(\zeta) \sim -\frac{U^2 a_m(t)^2 q_m^2 \mathrm{e}^{2\mathrm{i}\vartheta_m^-}}{\zeta-\zeta_m^-}\frac{\mathrm{d}^2\mathcal{Z}}{\mathrm{d}\zeta^2}(\zeta_m^-).$$

Applying the residue theorem to (F.4) yields the final expression for the leading edge suction force:

$$T_m^{(l)}(t) = \frac{1}{2}\mathcal{X}_m \pi U^2 a_m(t)^2 q_m^2 \mathrm{e}^{2\mathrm{i}\vartheta_m^-} \frac{\mathrm{d}^2\mathcal{Z}}{\mathrm{d}\zeta^2}(\zeta_m^-).$$

We recover the known leading-edge suction force for a single plate as $T_0^{(l)} = \pi U^2 a_0(t)^2/2$ when the map $\mathcal{Z}$ is taken to be the Joukowski map and the leading edge is $\zeta_0^- = \mathrm{e}^{2\mathrm{i}\vartheta_0^-} = -1$ [46, 62].

For harmonic motions we can similarly decompose the thrust averaged over a single period as $\langle T_m \rangle = \langle T_m^{(p)} \rangle + \langle T_m^{(l)} \rangle$ where

$$\left\langle T_m^{(p)} \right\rangle = -\frac{1}{2}\mathcal{X}_m \oint_{C_m} \left(\phi^c(\zeta) \frac{\mathrm{d}h_m^c}{\mathrm{d}x}(x(\zeta)) + \phi^s(\zeta) \frac{\mathrm{d}h_m^s}{\mathrm{d}x}(x(\zeta)) \right) \frac{\mathrm{d}\mathcal{Z}}{\mathrm{d}\zeta}(\zeta)\mathrm{d}\zeta, \tag{F.5}$$

$$\left\langle T_m^{(l)} \right\rangle = \frac{1}{4}\mathcal{X}_m \pi U^2 \left((a_m^c)^2 + (a_m^s)^2 \right) q_m^2 \mathrm{e}^{2\mathrm{i}\vartheta_m^-} \frac{\mathrm{d}^2\mathcal{Z}}{\mathrm{d}\zeta^2}(\zeta_m^-). \tag{F.6}$$

F.3 | Power

The power required to maintain the motion of the m-th wing is

$$P_m(t) = \int_{z_m^-}^{z_m^+} \Delta\phi_m(x,t) \frac{\partial h_m}{\partial t}(x,t)\mathrm{d}x,$$

which can be transformed into D_ζ:

$$P_m(t) = \mathcal{X}_m \oint_{C_m} \phi(\zeta,t) \frac{\partial h_m}{\partial t}(x(\zeta),t) \frac{\mathrm{d}\mathcal{Z}}{\mathrm{d}\zeta}(\zeta)\mathrm{d}\zeta.$$

For harmonic motions, the thrust averaged over a single period is

$$\langle P_m \rangle = \pi \mathcal{X}_m \oint_{C_m} \left(\phi^c(\zeta) h_m^s(x(\zeta)) - \phi^s(\zeta) h_m^c(x(\zeta)) \right) \frac{\mathrm{d}\mathcal{Z}}{\mathrm{d}\zeta}(\zeta)\mathrm{d}\zeta. \tag{F.7}$$

F.4 | Efficiency and kinetic energy

Two further important diagnostic quantities can be defined in terms of the thrust and power. First, the net propulsive efficiency of the system for producing thrust is [62, Eq. 55]

$$\eta_{\mathrm{net}} = \frac{U \sum_{m=0}^{M} \langle T_m \rangle}{\sum_{m=0}^{M} \langle P_m \rangle}. \tag{F.8}$$

Second, the time-averaged kinetic energy imparted to the fluid by the motion of the plates is [62, Eq. 43]

$$\langle E \rangle = \sum_{m=0}^{M} \langle P_m \rangle - U \langle T_m \rangle .$$